POLITECNICO DI TORINO

Master's Degree in Energy and Nuclear Engineering

Application of Fluent in Biomass Drying Simulation

Supervisors

Prof. Andrea LANZINI

Prof. Hervé JEANMART

Asst. Nicolas PARMENTIER

Candidate

Fabio FAULE

October 2024

Abstract

This thesis has been developed through a collaboration between Politecnico di Torino and Université Catholique de Louvain. It investigates the drying processes of biomass, specifically focusing on wood chips and sawdust, using ANSYS Fluent as computational fluid dynamics software. Biomass drying is a critical step in various industrial applications, particularly in bio-energy production, as it increases the fuel efficiency by reducing the moisture content. The research begins with an overview of common biomass drying technologies, including rotary, conveyor, and open-air drying systems, exploring their field of application and underlying principles of operation. The core of this work centers on the application of the Fluent software to model and simulate biomass drying processes. A multiphase Eulerian model was used, combined with the Lee model for evaporation-condensation, to accurately simulate the interaction between biomass and the airflow. The simulation results were compared with experimental data from the work of Bengtsson on low-temperature biomass drying. The results showed a close alignment between the simulation and experimental findings, validating the computational model. The study includes a case analysis of the drying system employed by Coopeos and Intradel, two organizations active in biomass energy in Belgium. The findings from this research contribute to enhancing biomass drying techniques and also highlight the potential for optimizing key parameters through the model, which could drive further improvements in similar facilities in the future.

Table of Contents

List of Tables

List of Figures

Chapter 1

Introduction

Biomass has emerged as a critical resource in the global shift towards renewable energy solutions. As a sustainable and widely available material, it offers significant potential for reducing reliance on fossil fuels and decreasing carbon emissions. Biomass is not only used for heating and electricity generation but also serves as a valuable input in various industrial processes. Among these, woody biomass, including wood chips and sawdust, is one of the most commonly utilized forms due to its accessibility and versatility [1].

A key step in the efficient use of biomass for energy and industrial applications is the drying process. Reducing the moisture content of biomass increases its lower heating value (LHV), improving its energy efficiency and making it a more effective fuel source. Dry biomass burns more efficiently, generates higher energy outputs, and reduces emissions, including harmful particulate matter and volatile organic compounds. Furthermore, drying biomass before combustion enhances heat production, reduces air emissions, and improves overall boiler operation. In boilers or gasifiers, moisture in the fuel must first be heated and evaporated, consuming significant amounts of energy. By removing moisture through a dedicated drying process, this energy loss is minimized. Although drying equipment also requires energy for heating and evaporating moisture, it operates more efficiently when designed specifically for this purpose. If the heat for drying can be recovered from other processes, such as boiler flue gas or gasifiers, the overall efficiency of the system is further increased. Additionally, proper drying minimizes the risk of fungal growth and decomposition, which can occur during storage or transportation when the biomass retains a high moisture content. As industries strive for more sustainable and cost-effective practices, optimizing biomass drying techniques has become increasingly important [2].

Despite its importance, biomass drying poses several challenges. The moisture content of biomass can vary significantly, and achieving an even and efficient drying process requires careful control of multiple parameters, such as temperature, airflow,

and humidity. Traditional drying methods, while widely used, may not always achieve the desired balance between energy consumption and drying efficiency. Furthermore, factors such as environmental conditions, biomass particle size, and storage configurations can impact the drying rate and overall effectiveness of the process[3].

This thesis aims to address these challenges by applying computational fluid dynamics using ANSYS Fluent to simulate the biomass drying process, with a particular focus on wood chips and sawdust. Through the development of a multiphase Eulerian model, coupled with the Lee model for evaporation and condensation, this research investigates the complex interactions between biomass and airflow during the drying process. The study draws on real-world case analyses, including the drying systems of Coopeos and Intradel, two organizations actively engaged in the field of biomass energy production in Belgium. By validating the simulation results against experimental data and analyzing the drying performance of an industrial system, this work aims to contribute to the improvement of biomass drying methods.

Chapter 2

Drying Technologies

Drying biomass, particularly wood chips, is a critical step in various industrial processes, including energy production, material processing, and environmental management. Effective drying reduces the moisture content of wood chips, enhancing their calorific value and making them more efficient as a fuel source. Additionally, drying minimizes the risk of fungal growth and other degradation processes that can occur in moist biomass, ensuring the material remains stable during storage and transportation. There are various methods for drying biomass, each tailored to specific needs based on the material's characteristics and the operational requirements of the facility. These methods are broadly categorized into direct-fired and indirect-fired types, each offering distinct advantages and suitable for different applications.

Direct-fired dryers are typically more efficient and faster, as the drying medium (usually hot air or flue gas) comes into direct contact with the biomass, quickly reducing its moisture content. This method is particularly well-suited for high-throughput operations where time and energy efficiency are critical. However, direct-fired dryers may require careful control to prevent scorching or uneven drying, especially with sensitive materials like wood chips.

Indirect-fired dryers, on the other hand, involve a heating medium that does not directly contact the biomass. Instead, heat is transferred through a barrier, such as tubes or a rotating drum, making this method more suitable for materials that are prone to contamination or require a more controlled drying environment. While indirect-fired dryers are generally slower and less energy-efficient than their direct-fired counterparts, they offer greater protection for the biomass and are often used in applications where product quality is paramount [3].

Among the technologies employed for drying wood chips, rotary, conveyor and open-air dryers are among the most prevalent. The choice of drying technology depends on factors such as the initial and final moisture content of the wood chips, the scale of operation, and the specific requirements of the end-use application.

2.1 Rotary Dryers

Rotary dryers are one of the most widely used type of dryer for biomass processing. Among the different variations, the directly heated single-pass rotary dryer showed in Figure 2.1, is the most commonly employed. In this type of dryer, hot gases are introduced into a rotating drum where they come into direct contact with the biomass. As the drum rotates, internal flights lift the material, causing it to cascade through the hot gases, thereby improving heat and mass transfer. If contamination is not an issue, hot flue gases can be fed directly into the dryer. Alternatively, a burner may be used to raise the temperature of the air entering the system.

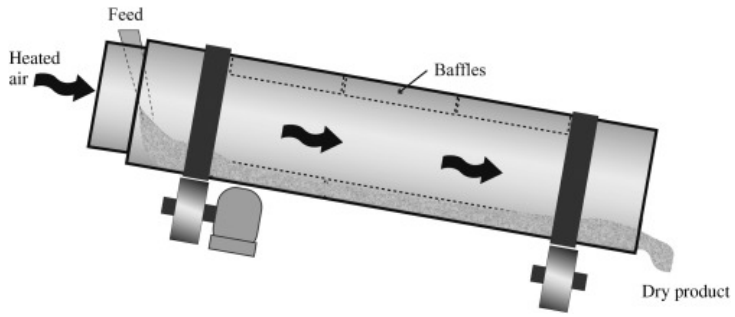

Figure 2.1: Schematic of a rotary dryer. Heated air is introduced at the feed side, and internal baffles facilitate mixing as the material moves through the drum, exiting as a dry product. [4]

Typically, the biomass and hot air flow co-currently through the dryer, meaning the hottest gases interact with the wettest material. However, when temperature sensitivity is not a concern, the gases and solids can flow in opposite directions, allowing the driest material to meet the hottest gases, thus achieving the lowest moisture content at the dryer's exit. This latter setup, however, poses a higher fire risk as it exposes nearly dry material to high flue gas temperatures. The exhaust gases from the dryer often require treatment to remove fine particles before release. This may involve passing through equipment such as a cyclone, baghouse filter, scrubber, or electrostatic precipitator (ESP).

The design of a single-pass rotary dryer can be adapted to allow the material and air to pass through the system multiple times. Initially, the material enters an inner cylinder where it contacts hot air. Smaller or drier particles are quickly moved through this cylinder into a larger outer cylinder for a second pass, while larger material is tumbled with the aid of flights. After the second pass, the material and air pass through the outermost cylinder before exiting the dryer. This triple-pass configuration is best suited for materials smaller than few centimeters (like sawdust and tiny woodchips), as larger particles can cause clogging, whereas single-pass dryers are capable of handling larger materials.

2.2 Conveyor Dryers

Conveyor dryers operate by spreading feedstock onto a moving perforated conveyor, which allows for continuous drying. Fans are used to blow the drying medium through the conveyor and the material, either from above or below. When multiple conveyors are employed, they can be arranged in series or stacked in a "multi-pass" configuration. Although conveyor dryers are less commonly used for drying materials like bark and shredded wood waste, which are processed through mechanical shredders or grinders, they are highly versatile and can accommodate a wide range of materials. These dryers present several advantages and some drawbacks when compared to the more commonly used rotary dryers [3].

A significant benefit of conveyor dryers is their ability to capitalize on waste heat recovery due to their lower operating temperatures compared to rotary dryers. Rotary dryers generally require inlet temperatures starting at 260°C, with optimal operation around 400°C. In contrast, some vacuum conveyor dryers can function with inlet temperatures just slightly above ambient, though more typically, they operate between 90°C and 200°C. This lower temperature range makes conveyor dryers ideal for integration with boiler stack economizers, where heat is first recovered from boiler flue gases and then used for fuel drying. The lower operating temperatures of conveyor dryers also offer a reduced fire hazard and lower emissions of volatile organic compounds (VOCs). Another advantage is that the material remains stationary during the drying process, which can result in fewer particulate emissions. However, fines may need to be screened out before drying and reintroduced later, as they can fall through the perforations in the conveyor belt.

Single-pass conveyor dryers generally require more space than rotary dryers of a similar capacity. However, multi-pass conveyor dryers, where conveyors are stacked with material cascading down from upper to lower conveyors, are more space-efficient. Due to their smaller footprint and cost-effectiveness, multi-pass conveyor dryers are widely used across various industries.

In a classic single pass conveyor dryer, the wet biomass enters the system (1) depicted in figure 2.2, a feeding screw (2) is responsible for the leveraging of the product on the belt. The air pulled by the fan (6) passes through the heat exchanger (5) is being heated, afterwards it goes across the product and the belt exiting from the chimney. At the end of the belt the dry biomass is helped by the cleaning brush to exit (3,8) and the washing device (9) is able to restore the initial condition of the conveyor.

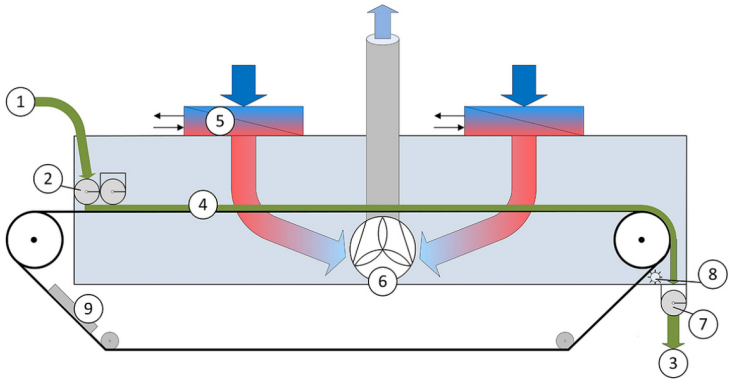

Figure 2.2: Conveyor drying system scheme: 1.Wet product, 2.Feeding screw, 3.Dry product (discharge), 4.Even product layer, 5.Heat exchangers, 6.Main fan, 7.Discharge screw, 8.Cleaning brush, 9.Belt washing device [5]

2.3 Open Air Drying

Open-air drying, also known as natural or passive drying, is a traditional and widely used method for reducing the moisture content of woody biomass (Figure 2.3). This technology is particularly favored in regions with favorable climatic conditions due to its simplicity, low operational costs, and minimal energy requirements. Unlike artificial drying methods that rely on mechanical equipment and external energy sources, open-air drying harnesses natural elements such as wind, sunlight, and ambient temperature to gradually remove moisture from biomass materials.

The process typically involves spreading or stacking woody biomass, such as logs, branches, or wood chips, in well-ventilated outdoor areas. The biomass is exposed to the open air, allowing moisture to evaporate over time. Key factors that influence the efficiency of open-air drying include the arrangement and size of the biomass, the duration of exposure, and local weather conditions such as humidity, temperature, and wind speed. Proper stacking techniques, such as placing wood in cross-piles or aligning logs to maximize airflow, are crucial to enhancing drying rates and preventing issues like mold growth or uneven drying.

When it comes to sawdust and wood chips, the open-air drying process becomes more complex due to the smaller particle size and increased surface area per unit of volume which require increased exposure to airflow for effective drying. Sawdust and wood chips, tend to hold moisture more tenaciously and can form dense piles that limit airflow, leading to slower drying rates and a higher risk of fungal growth and decomposition.

For sawdust, frequent turning or stirring of the sawdust is often necessary to ensure even drying and to prevent compaction, which can trap moisture and slow

down the process. Additionally, protective coverings may be used during periods of rain or high humidity to prevent the reabsorption of moisture.

Wood chips, while less prone to compaction than sawdust, still require careful management in the drying process. Piles of wood chips should be kept relatively shallow and well-ventilated to promote airflow. Some techniques involve the use of perforated floors or raised platforms to allow air circulation from below, further enhancing the drying efficiency. The shape and size of the wood chips also play a role; smaller or irregularly shaped chips dry faster but may also require more frequent handling to prevent issues such as spontaneous combustion, which can occur if heat builds up within a poorly ventilated pile.

Figure 2.3: Picture of an Open-air drying plant featuring a roof and covered on three sides[6]

More complex versions of open-air drying are commercially available, offering a range of enhancements that significantly improve efficiency and meet specific needs. One of the most common and straightforward improvements is the addition of a cover to protect the biomass from environmental factors . Another frequent enhancement is the implementation of mechanical ventilation to accelerate the drying process. Additionally, the biomass can be elevated, or aeration channels may be installed beneath it to further improve airflow and ensure more uniform drying (figure 2.4).

Unlike natural seasoning, warm air-drying—such as in a convective dryer—offers distinct benefits. It provides more effective moisture removal, better control over the drying process, and ensures the biomass meets specific quality and storage requirements. In these systems, ventilation can be enhanced by incorporating heat

from various sources, such as waste heat from industrial processes, dedicated boilers, or heat exchangers. Utilizing waste heat from industrial sources or other processes to warm the air through heat exchangers is a common practice. This method efficiently recycles energy that would otherwise be lost, thereby lowering overall energy consumption and reducing operational expenses. With the introduction of solar collectors to boost the drying process, the system becomes less dependent on ambient conditions compared to traditional seasoning methods [7]. Although the initial investment in solar collectors is higher than that for traditional boilers, they offer significantly lower environmental impact, making them an sustainable long-term solution.

Figure 2.4: Picture of an open air drying plant with mechanical turning [8]

Figure 2.5: Picture of a solar based open air drying plant (equipped with solar-air collectors) [9]

Chapter 3

Case Study: Coopeos & Intradel

This work focuses on two key organizations: Coopeos and Intradel, both of which play significant roles in the field of biomass transformation and utilization in Belgium.

3.1 Coopeos

Coopeos is a Belgian cooperative involved in the design and installation of biomass-based thermal systems, particularly wood-fired boilers. The organization's mission is to enhance the value of local wood resources by promoting sustainable heating solutions for buildings. This involves transforming these resources into high-quality wood chips for wood boilers, as well as designing, installing, financing, and managing the boilers. Additionally, Coopeos is dedicated to raising awareness about sustainable development among a broad audience. The cooperative provides customer support and maintenance services, and although it is a relatively small enterprise it has established itself in the *Région wallonne*, with a portfolio of approximately 50 installations spread across schools, sports centers and residential sites [10]. The cooperative's design approach is notable for its use of repurposed shipping containers to house entire customized installations. This strategy facilitates transportation and reduces the need for specialized labor at the installation site. In response to the growing demand for higher-quality biomass with improved energy efficiency, Coopeos's research department is currently focusing on the drying of woody biomass. By reducing the moisture content, they aim to increase the calorific value of the wood, making it a more efficient fuel source. Consequently, this study will closely examine the methods and outcomes associated with the drying of woody biomass.

3.2 Intradel

Intradel is another key player, which mission focuses on sustainable waste management by promoting recycling and responsible waste treatment, while also raising public awareness about environmental protection. Additionally, their management of waste and recycling facilities provides access to a significant supply of biomass that can be economically leveraged. Intradel is focused on the collection and processing of green waste, including sorting, cleaning, cutting, grinding, sizing (with the relevant size range being 6-40 mm for this work), drying, and distribution for energy production. The organization operates a facility specifically designed for open-air drying of biomass, which is central to this study. Unlike standard open-air drying setups, Intradel's facility includes an aeration system located beneath the ground level, enhancing the drying process. The facility also features a transparent cover that protects the biomass from adverse weather conditions, ensuring consistent drying performance. At the time of the site visit, this cover was being replaced in preparation for the upcoming season. To provide a clearer understanding of the infrastructure and layout of the Intradel facility, an image of the drying plant is presented below. This image highlights the key components of the system, including the underground aeration ducts and the transparent protective cover.

Figure 3.1: Intradel silo under study in this thesis, shown during the cleaning phase. The metal grates have been temporarily removed from the air ducts for maintenance

This thesis will focus on the drying system employed at the Intradel facility, exploring its design and operational efficiency. The following section will provide a detailed analysis of the system, accompanied by schematics to illustrate its components and functionality.

3.3 Open-air drying plant

The image 3.2 illustrates a top view of the Intradel drying silo, showcasing its structural and functional elements. The walls of the silo, depicted in pink, are constructed from prefabricated concrete blocks, forming the sturdy enclosure necessary for the structural support and containment of the biomass. The green lines represent the air ducts and the black lines indicate the dimensions of the various components expressed in centimeters.

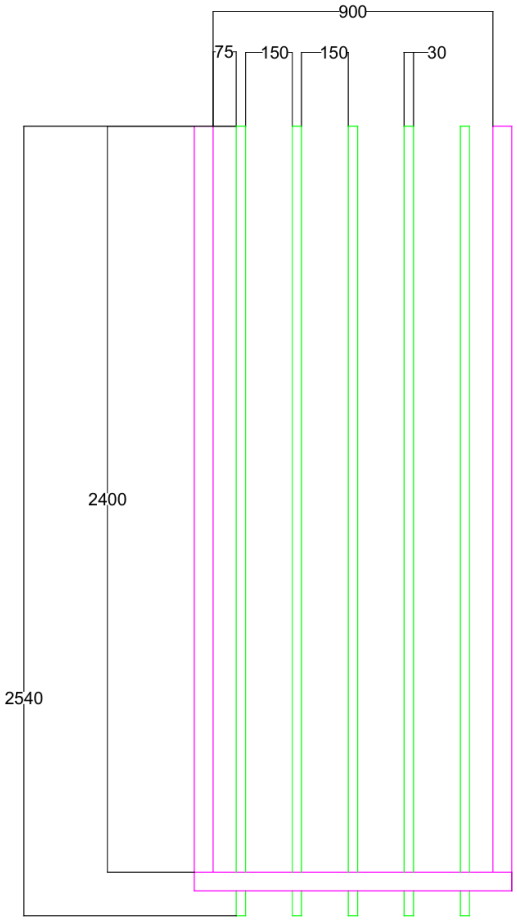

Figure 3.2: Technical drawing of the Intradel silo, top view section showing internal layout and dimensions

In the subsequent Figure 3.3, a cross-sectional view of the silo is presented, focusing specifically on one of the aeration channels. This section provides a detailed look at the design and dimensions of the air channel, highlighting its role in the overall ventilation system within the silo.

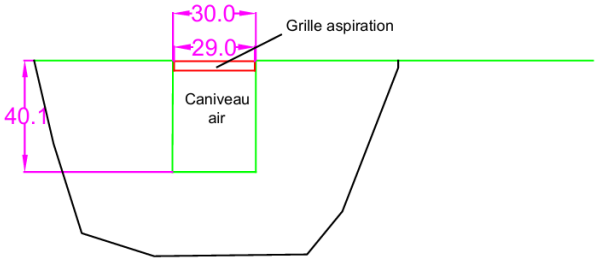

Figure 3.3: Technical drawing of the Intradel silo, showing a cross-section at ground level and below. The diagram illustrates the shape and dimensions of the air ducts, as well as the size and placement of the aspiration grates

The plant under study includes a customized container housing a woodchip-fired boiler, a fan, a damper system, and various sensors and control units to manage and regulate the entire system. A simplified diagram of the plant is provided in Figure 3.4

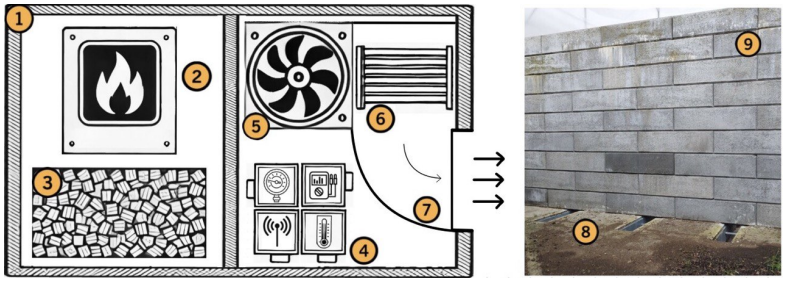

Figure 3.4: Conceptual diagram of the customized Coopeos container. 1.Container frame 2.Boiler 3.Woodchip storage 4.Electrical control system, equipped with various sensors and data-sharing mechanisms 5.Fan 6.Damper system 7.Air ducts 8.Connection to the plant's air channels 9.Rear wall of the plant

The fan is installed inside the customized container alongside the boiler and, through the system of dampers, allows for the air to be either pushed into or drawn out of the ducts. The fan is connected to the ventilation system of the facility via metal pipes on the exterior, where the aeration channels extend beyond the containment wall at the furthest point from the entrance of the structure. The design of this system enables dual functionality, depending on weather conditions, operational needs, and the thermophysical properties of the surrounding air. This allows for two distinct modes: winter and summer. In winter mode, the boiler inside

the container burns biomass to produce hot water, which is then sent to a heat exchanger to generate warm air. The fan pushes this warm air through the facility's ducts, gradually heating the biomass from below, as will be further analyzed in the following chapters. In summer mode, the ventilation system operates in reverse. Air is drawn from the area where the biomass is located and expelled outside. With the presence of sunlight, the transparent cover allows solar radiation to heat the upper surface of the biomass. This cover also helps retain the warm air that forms. The fan then removes the air, which by this point contains a high level of water vapor, from the silo, promoting effective drying.

The complete technical datasheet for the installed centrifugal fan is provided at [11]. Below in Figure 3.5 the performance graph is presented. The perfomance graph is the tool for understanding how the fan will behave under various operating conditions. Indeed, the relation between pressure, airflow, and rotational speed is illustrated. Each curve on the graph corresponds to a specific fan speed, measured in revolutions per minute (RPM), and shows how the airflow (measured in cubic meters per second) varies with pressure (measured in Pascals).

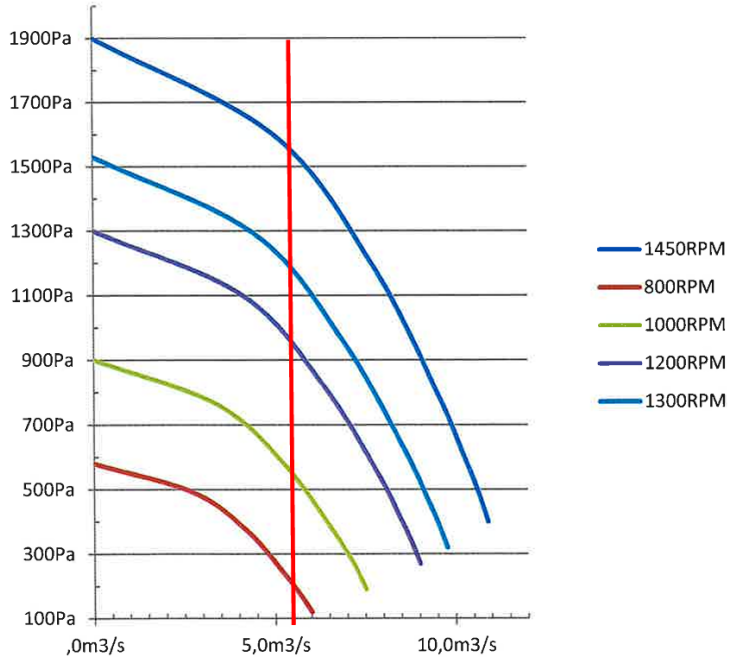

Figure 3.5: Performance graph - GROS 1RV1-11 [6]

In winter mode, the boiler is activated to burn wood chips, producing hot air via a heat exchanger (HE). This hot air is then pushed by the fan into the ducts, where it reaches the biomass that needs to be dried.

It is important to note that the pressure drop in the model is accounted for and not assumed to be zero. However, for the purposes of this study, the fan is considered capable of maintaining a constant flow rate, regardless of the pressure drop. The pressure drop caused by approximately 4.5 meters of wood chips can affect the fan's volume flow rate, which in turn might influence the temperature of the hot air. To evaluate the drying model developed in Fluent, the following nominal operating parameters (Table 3.1) are assumed as constants and applied directly in the software.

Nominal condition	
Volume Flow rate	5.5 m^3/s
Temperature of the air - Ambient	5 $°C$
Relative Humidity of the air - Ambient	60 %
Temperature of the air - after HE	43 $°C$
Relative Humidity of the air - after HE	6 %

Table 3.1: Nominal condition of the plant in winter mode

Chapter 4

Theory and Model Assumptions

Consider a batch containing moist, solid, and irregularly shaped biomass particles, such as sawdust, wood chips, or bark. These particles constitute a porous mixture comprising both solid material and a gas phase (humid air). To facilitate the drying process, a stream of hot air is passing through the porous structure. As the hot air interacts with the moist particles, moisture is transferred to the air. This process is depicted in Figure 4.1.

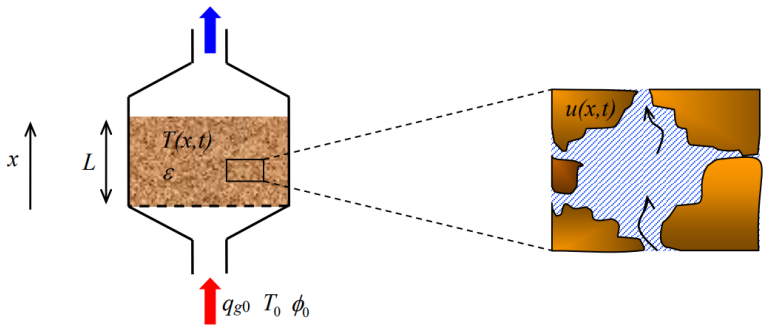

Figure 4.1: Setup for the model of drying biomass [12]

Where the height of the bed is denoted as L, the moisture content of the solid particles is represented by $MC(x,t)$ (in kg_w/kg_{ds}), and their temperature is denoted by $T(x,t)$ (in $°C$). Furthermore, x represents the vertical position and t represents time, the porosity of the bed is defined as ε (in m^3_{void}/m^3_{tot} cubic meters of void space per cubic meter of batch). The inlet volumetric air flux is denoted as q_{g0} (in $m^3/m^2\ s$), with the inlet gas having a relative humidity of RH_0 (indicated with φ_0 in Figure 4.1) and a temperature of T_0 (in $°C$).

4.1 Moisture Content and Fiber saturation point

The moisture content (MC) of the solid material, measured in kilograms of water per kilogram of dry solid (kg_w/kg_{ds}), is defined as the ratio of the mass of moisture (m_w) to the mass of dry matter (m_{ds}) within the material [12]:

$$MC = \frac{m_w}{m_{ds}} \tag{4.1}$$

where m_{ds} is the mass of the oven-dried wood. In practice, the moisture content of a given piece of wood can be calculated by:

$$MC = \frac{m_{wet} - m_{ds}}{m_{ds}} \tag{4.2}$$

where m_{wet} is the mass of the specimen at the given MC condition. In wood, moisture can be present as either free water (liquid water or vapor within the cells and cavities) or bound water (water retained within the cell walls through intermolecular forces). The moisture content at which the cell walls are fully saturated with bound water, but no free water remains in the cell lumina, is known as the fiber saturation point (MC_{fs}). The Fiber Saturation Point (FSP) is a critical threshold in wood science, it generally occurs when the moisture content is between 25% and 30%. This point can vary slightly depending on the wood species, but the overall concept remains consistent. Below the FSP, the moisture in the wood is primarily in the form of bound water within the cell walls. Above the FSP, any additional moisture is free water found in the cell cavities. This free water does not significantly affect the mechanical properties or dimensional stability of the wood but impacts other aspects such as weight [13]. Therefore, conceptually, the fiber saturation point serves as the dividing line between the two forms in which water is retained within wood.

4.2 Density and Bulk density

The intrinsic density of wood, while influenced by the moisture content, can be determined through various experiments, one of which is helium pycnometry. This technique, based on the principle of gas displacement, allows for an accurate measurement of the true volume of the wood. The density obtained through this method does take into account the interstitial pores present inside the wood, effectively reducing the considered volume, especially in the case of highly porous woods. Throughout this work, the wood density will be denoted as ρ_w, which typically ranges from 1300 kg/m^3 to 1500 kg/m^3, as it has been found in the study of Horabik Et al. [14].

Bulk density (BD), on the other hand, is the density of wood that can be measured without the need for complex methodologies. It is determined by weighing and measuring the dimensions of the specimens under consideration. Bulk density varies significantly depending on the form of the wood (e.g., sawdust, wood chips, pellets, whole wood, etc.), for most species in ovendry situation it can range between 200 kg/m^3 and 800 kg/m^3 [13]. The volume considered in bulk density calculations includes the volume of the pores within the wood and the volume due to the packing of the biomass. For materials like sawdust, wood chips, or pellets, bulk density can be measured under different levels of pressure to account for varying storage methods [14].

In this context, bulk density varies significantly and, like ρ_w, is affected by moisture content. For wood chips, bulk density is also highly dependent on the porosity of the packed bed. Several studies have examined the bulk density of wood chips in piled storage [15]. The most relevant large-scale estimates of woodchip bulk density come from cone-shaped stockpiles at wood recycling facilities, with reported values of 210 and 230 kg/m^3 from Amato et al. (2020) [16] and 245 ± 49 kg/m^3 from Subroy et al. (2014) [17].

4.3 Porosity

Porosity is a defining characteristic of materials containing both solid components and void spaces, serving as a metric for the extent of these voids. Complex materials such as wood chips and sawdust exhibit porosity at multiple scales. Firstly, at a microstructural level, the porous nature of wood arises from its intricate composition of cell walls and lumens. Furthermore, when aggregated together, wood particles collectively contribute to porosity, forming a heterogeneous mixture of solid wood particles interspersed with interstitial pore spaces [12]. The porosity (ε), measured in cubic meters of void space per cubic meter of particles (m^3/m^3), characterizes the packing density of a bed of particles and is defined as:

$$\varepsilon = \frac{V_g}{V_g + V_s} \tag{4.3}$$

Here, V_g represents the pore volume (m^3) where the gas streams, while V_s denotes the volume occupied by the solid material (m^3). Therefore, the total bulk volume is the sum of V_g and V_s. Alternatively, porosity can be calculated using the definition of bulk density:

$$\varepsilon = 1 - \frac{BD}{\rho_w} \tag{4.4}$$

4.4 Evaporated water

When performing biomass drying, there is an initial moisture content (MC_0) and a desired final moisture content (MC_{final}). Based on this, it is possible to calculate the amount of water that needs to be evaporated, and consequently, the theoretical minimum energy required to evaporate that water. This theoretical energy can then be compared with the actual energy used to transition from the initial MC to the final MC. The amount of water evaporated can be calculated as:

$$\begin{aligned} m_{lw} &= m_{w0} - m_{w-final} = \\ &= m_{ds} \frac{MC_0 - MC_{final}}{100} = \\ &= \rho_w \, V_{tot} \, (1 - \varepsilon) \frac{MC_0 - MC_{final}}{100} \end{aligned} \tag{4.5}$$

4.5 Homogeneous Temperature

The temperature within the solid is assumed to be uniform, with no heat flux occurring inside the particles. This indicates that the Biot number (Bi), which compares the heat transfer at the particle's surface to that within the particle itself, is close to zero. The Bi is a dimensionless parameter, defined as:

$$Bi = \frac{hL_c}{k} \tag{4.6}$$

where L_c is the characteristic length (often the volume-to-surface-area ratio), and k is the material's thermal conductivity. A Biot number smaller than 1 suggests that heat conduction inside the particle is much faster than heat transfer at the surface, resulting in a nearly uniform temperature within the particle. A low Biot number (less than 1) indicates that the internal resistance to heat conduction is negligible compared to the heat transfer at the surface, resulting in a nearly uniform temperature throughout the material. In contrast, a high Biot number (greater than 1) suggests significant internal temperature gradients, with the material being thermally thick. Since wood is a material with insulating properties, its thermal conductivity is among the lowest. Therefore, in this situation, the problem is thermally thick (i.e., $Bi > 1$), and assuming a constant temperature is an approximation. However, in this scenario, the energy within the wood is primarily used to dilute the energy of the fluid phase. Consequently, the temperature distribution inside the particle is not of special interest.

4.6 Heat Capacity of the wood

Heat capacity refers to the amount of energy required to raise the temperature of a unit mass (kg) by one degree (K or $°C$). For wood, the heat capacity is influenced by both its temperature and moisture content, although it remains relatively unaffected by the density or species of the wood [13]. The heat capacity of dry wood, denoted as c_{p-ds} (in $kJ/kg\ K$), can be estimated as a function of temperature T (in K) using the following expression:

$$c_{p-ds} = 0.1031 + 0.003867\,T \tag{4.7}$$

Furthermore, when wood contains moisture, its heat capacity increases. Below the fiber saturation point, the heat capacity is a combination of the heat capacity of dry wood and that of water (c_{pw}), with an adjustment factor accounting for the extra energy involved in the wood-water bond. Above the fiber saturation point, the additional moisture influences the heat capacity according to the principle of simple mixtures [13].

4.7 Humid Air

Humid air is composed of a mixture of dry air and water vapor. Dry air refers to the combination of all the gases in the atmosphere (such as nitrogen, oxygen, carbon dioxide, and noble gases), with the exception of water vapor. Since the subject of study is humid air under conditions where the pressure is very close to atmospheric pressure and the temperature is similar to ambient conditions (along with the fact that water vapor has a relatively low partial pressure compared to other gases present, and intermolecular forces are sufficiently weak under these circumstances), it is assumed that humid air behaves according to the ideal gas laws. Indeed, an ideal gas adheres to the general gas law, expressed as:

$$P\ V = n\ R\ T_K \tag{4.8}$$

Here, P stands for the total pressure (Pa), V for the volume (m^3), n for the number of moles of gas, $R = 8.314$ for the gas constant ($J/mol\ K$), and T_K for the absolute temperature (° K). The moles of gas, n, can be defined as $n = \frac{m}{M}$, where m denotes the mass (kg) and M represents the molar mass kg/mol [12]. The density ρ (kg/m^3) equals (m/V), and the general gas law can be reformulated as:

$$\frac{P}{R\ T_K} = \frac{\rho}{M} \tag{4.9}$$

Humid air can be considered a mixture of at least two ideal gases: dry air with a molar mass $M_{da} = 0.029\ kg/mol$ and water vapor with $M_v = 0.018\ kg/mol$.

The molar mass of dry air depends on its composition, which for standard air is approximately 79% nitrogen and 21% oxygen [18]. The partial pressures of air, p_{da}, and vapor, p_{wv}, are given by:

$$p_{da} = \frac{R\ T_K\ \rho_{da}}{M_{da}}, \quad p_{wv} = \frac{R\ T_K\ \rho_{wv}}{M_{wv}} \tag{4.10}$$

Here, ρ_{da} represents the dry air density and ρ_{wv} is the water vapor density, also referred to as specific humidity (kg/m^3). Dalton's law of partial pressure states that the total pressure P of a gas equals the sum of the partial pressures p_n exerted by its components. For humid air, Dalton's law yields:

$$P = p_{da} + p_{wv} \tag{4.11}$$

The density of humid air can be directly computed as the sum of the partial densities of the dry air and the water vapor:

$$\rho_{ha} = \rho_{da} + \rho_{wv} \tag{4.12}$$

4.8 Absolute and Relative Humidity

Absolute humidity, denoted by x, is defined as the ratio of the mass of water vapor to the mass of dry air within a given volume. Mathematically, it is expressed as:

$$x = \frac{m_{wv}}{m_{da}} \tag{4.13}$$

where m_{wv} is the mass of water vapor, and m_{da} is the mass of dry air. Alternatively, absolute humidity can be written in terms of the partial densities of water vapor (ρ_{wv}) and dry air (ρ_{da}):

$$x = \frac{\rho_{wv}}{\rho_{da}} \tag{4.14}$$

Furthermore, using the concept of partial pressures, absolute humidity can be expressed as a function of the partial pressure of water vapor and the partial pressure of dry air. Given the difference in molar masses between water vapor and dry air, a proportionality factor is introduced, yielding the following equation:

$$x = 0.622\,\frac{p_{wv}}{p_{da}} = 0.622\,\frac{p_{wv}}{p - p_{wv}} \tag{4.15}$$

This relationship allows for the calculation of absolute humidity using only the partial pressures. Solving for p_{wv}, we can determine the partial pressure of water vapor:

$$p_{wv} = \frac{x}{0.6220 + x}\, p \tag{4.16}$$

On the other hand, relative humidity (RH) is defined as the ratio of the partial pressure of water vapor in the air to the saturation vapor pressure at a given temperature. Expressed as a percentage, relative humidity indicates how close the air is to being fully saturated. At 100% relative humidity, the air is saturated, and any additional water vapor will condense into liquid form. The RH serves as a measure of humidity in the drying air. It can be computed as:

$$RH = \frac{p_{wv}}{p_{\text{wv-sat}}(T)} \tag{4.17}$$

In theory the value of $p_{\text{wv-sat}}$ is not only a function of T but also of but as it has been proved by [18], the pressure in saturation condition of water vapour only slitghtly depends on the presence of the dry air in the ambient gas. In the drying process of woodchips, controlling relative humidity is essential, as high humidity levels slow down evaporation, making the process less efficient and prolonging the drying time.

Chapter 5

Fluent Model

This chapter will describe the methodology used to simulate the biomass drying process, specifically woodchips and sawdust, using ANSYS Fluent software [19]. Fluent is a powerful Computational Fluid Dynamics (CFD) tool that enables the analysis and understanding of complex phenomena involving mass, energy, and momentum transfer even in various phases. To accurately model the drying process of woodchips, a multiphase approach is adopted. Specifically, the Eulerian model is employed, allowing the interaction between the solid (biomass) and the fluids (humid air and liquid water) to be described. This is essential for simulating the heat and moisture transport mechanisms. The model also incorporates the Ranz-Marshall correlation to calculate heat transfer coefficients, while accounting for the flow dynamics through a porous medium, such as woodchips. In addition to the multiphase model, the Lee evaporation-condensation model is implemented to describe the phase transition between liquid water and vapor. Furthermore, the Ergun equation is applied to evaluate pressure drop in the porous medium [20]. Its important to specify that, the solid material, specifically the wood, is introduced into Fluent solely through the definition of porosity. In practice, Fluent does not treat the solid as physically present, but rather as a dilution of the energy and volume within the multiphase mixture. Additionally, the solid is modeled as a momentum sink in the momentum conservation equations, and it significantly impacts the pressure losses occurring within the region defined as porous. Throughout this chapter, the theoretical foundations behind each model will be discussed, explaining how they have been used to build the simulation of the biomass drying process.

5.1 Multiphase - Eulerian model

The Eulerian multiphase model in ANSYS Fluent is a powerful framework designed to simulate the behavior of multiple interacting phases, which can be liquid, gas, or solid. The Eulerian model treats each phase as interpenetrating continua, solving conservation equations for mass, momentum, and energy for each phase. This model is particularly suitable for flows where the interactions between phases are significant, such as in the drying processes of lignocellulosic fibrous material where moisture (liquid phase) evaporates into an airflow (gas phase). [21]

The Eulerian multiphase model allows for the simulation of an arbitrary number of secondary phases, provided sufficient memory and computational resources are available. The humid air phase is modeled using the species transport model, representing a mixture of water vapor and air. One of the key characteristics of the Eulerian model is that all phases share a common pressure field, simplifying the interaction between the phases. The exchange of momentum and energy between the phases is managed through interphase exchange terms, which account for forces like drag and pressure differences between them. This makes the model particularly suited for processes involving phase change, such as evaporation during drying. In this scenario, liquid water remains stationary in the porous medium, while humid air flows through, absorbing the evaporated water vapor and carrying it away from the material. The ability to fix the velocity of the liquid water phase within the porous structure, meaning it does not move during the simulation, is an important advantage of the Eulerian model [22]. Indeed, this behavior is critical in drying processes and other models do not offer this flexibility, making the Eulerian model particularly well-suited as it accurately simulates the stationary nature of the liquid phase while allowing the gas phase to flow freely through the medium.

5.1.1 Volume Fraction Equation

The description of multiphase flow as interpenetrating continua incorporates the concept of phasic volume fractions, denoted as α_q. Volume fractions represent the space occupied by each phase, and the conservation laws of mass and momentum are satisfied by each phase individually [22]. The derivation of the conservation equations can be performed using the mixture theory approach. The volume of phase q, V_q, is defined by:

$$V_q = \int_V \alpha_q dV \tag{5.1}$$

Where the sum of the volume fractions for all phases must satisfy the condition:

$$\sum_{q=1}^{n} \alpha_q = 1 \tag{5.2}$$

For the specific case of two phases, humid air (denoted as α_{ha}) and liquid water (denoted as α_{lw}), the equation becomes:

$$\alpha_{\text{ha}} + \alpha_{\text{lw}} = 1 \tag{5.3}$$

5.1.2 Conservation of Mass

The Conservation of Mass principle is fundamental in fluid dynamics and multiphase modeling. It ensures that the total mass in a system remains constant over time unless there is a source or sink of mass (e.g., due to phase change or reactions). For multiphase flow, each phase must individually satisfy the conservation of mass [22]. For a single phase q, the general conservation of mass equation can be written as:

$$\frac{\partial(\alpha_q \rho_q)}{\partial t} + \nabla \cdot (\alpha_q \rho_q \vec{v}_q) = \sum_{p=1}^{n} (\dot{m}_{pq} - \dot{m}_{qp}) + S_q \tag{5.4}$$

In this equation, α_q is as in 5.2. The term ρ_q refers to the density of phase q, while $\vec{v}_q$ is the velocity vector of that phase. The left-hand side of the equation describes the rate of change of the mass of phase q over time, combined with the mass flux as it moves through space. The right-hand side of the equation includes the mass transfer terms $\dot{m}_{pq}$ and $\dot{m}_{qp}$, which account for the mass being transferred from phase p to phase q and from phase q to phase p, respectively. These terms are critical in describing phase interactions, such as evaporation or condensation. The sum $\sum_{p=1}^{n}$ includes all other phases interacting with phase q. Lastly, S_q is a source term that represents external contributions or sinks of mass, and by default it is set to zero unless additional sources are specified in the system. This equation is particularly crucial for simulating drying processes, where mass is transferred between liquid water and humid air. In this context, the term $\dot{m}_{pq}$ represents the evaporation of liquid water into the gas phase, while $\dot{m}_{qp}$ account for condensation. For the specific case of two phases, humid air and liquid water, the conservation of mass equations take the following forms:

$$\frac{\partial(\alpha_{\text{ha}} \rho_{\text{ha}})}{\partial t} + \nabla \cdot (\alpha_{\text{ha}} \rho_{\text{ha}} \vec{v}_{\text{ha}}) = \dot{m}_{\text{lw}\to\text{ha}} - \dot{m}_{\text{ha}\to\text{lw}} \tag{5.5}$$

$$\frac{\partial(\alpha_{\text{lw}} \rho_{\text{lw}})}{\partial t} + \nabla \cdot (\alpha_{\text{lw}} \rho_{\text{lw}} \vec{v}_{\text{lw}}) = -\dot{m}_{\text{lw}\to\text{ha}} + \dot{m}_{\text{ha}\to\text{lw}} \tag{5.6}$$

The mass transfer term $\dot{m}_{\text{lw}\to\text{ha}}$ represents the rate of evaporation of liquid water into the humid air phase. As liquid water evaporates, its mass decreases, which is reflected as a negative term in the liquid water equation, while it adds mass to the humid air, resulting in a positive term in the corresponding equation. However, it is important to note that the opposite process, condensation, can also occur. In

this case, the term $\dot{m}_{\text{ha}\to\text{lw}}$ becomes significant, indicating the transfer of mass from humid air to liquid water. During condensation, the mass of humid air decreases, and that of liquid water increases. Since in each cell of the meshgrid all mass and energy balances are computed, the equation can take different values depending on the conditions within the specific cell. For instance, evaporation may dominate in some cells, while condensation may prevail in others, leading to variable system behavior and different solutions based on the spatial and temporal distribution of temperature and pressure conditions across the computational domain.

The S_q terms have been simplified, as there are no sources or sinks present in the system. Furthermore, the equation for liquid water can be simplified by noting that the velocity of the water has been set to $\vec{v}_q = 0$, which reduces the equation to:

$$\frac{\partial(\alpha_{\text{lw}}\rho_{\text{lw}})}{\partial t} = -\dot{m}_{\text{lw}\to\text{ha}} + \dot{m}_{\text{ha}\to\text{lw}} \tag{5.7}$$

5.1.3 Conservation of Momentum

The conservation of momentum equation describes how the momentum of each phase changes due to various forces, including pressure, body forces (such as gravity), and interphase interactions like drag. In multiphase flows, each phase has its own momentum equation, and interactions between phases are accounted for by interphase momentum transfer terms [22]. The general conservation of momentum equation for a given phase q is expressed as:

$$\begin{aligned}\frac{\partial(\alpha_q\rho_q\vec{v}_q)}{\partial t} + \nabla\cdot(\alpha_q\rho_q\vec{v}_q\vec{v}_q) = -\alpha_q\nabla p + \nabla\cdot\overline{\tau_q} + \alpha_q\rho_q\vec{g} + \\ \sum_{p=1}^{n}\left(\vec{R}_{pq} + \dot{m}_{pq}\vec{v}_{pq} - \dot{m}_{qp}\vec{v}_{qp}\right) + \left(\vec{F}_q + \vec{F}_{\text{lift},q} + \vec{F}_{\text{vm},q} + \vec{F}_{\text{td},q}\right)\end{aligned} \tag{5.8}$$

In this equation, the term $\alpha_q\rho_q\vec{v}_q$ represents the momentum of phase q, and the first term on the left-hand side describes the rate of change of momentum over time. On the right-hand side, the term $-\alpha_q\nabla p$ accounts for the pressure gradient force, and $\overline{\tau_q}$ represents the stress-strain tensor. The gravitational body force is given by $\alpha_q\rho_q\vec{g}$. The summation term represents interphase momentum transfer, where $\vec{R}_{pq}$ denotes the drag force between phases p and q, and $\dot{m}_{pq}\vec{v}_{pq} - \dot{m}_{qp}\vec{v}_{qp}$ accounts for the momentum transfer due to mass exchange between the phases. Where, the interphase velocity, denoted as $\vec{v}_{pq}$, is defined as follows. If $\dot{m}_{pq} > 0$ (indicating that mass is being transferred from phase p to phase q), then $\vec{v}pq = \vec{v}_p$. On the other hand, if $\dot{m}_{pq} < 0$ (indicating that mass is being transferred from phase q to phase p), then $\vec{v}_{pq} = \vec{v}_q$. Similarly, if $\dot{m}_{qp} > 0$, the velocity $\vec{v}_{qp} = \vec{v}_q$, and if $\dot{m}_{qp} < 0$, then $\vec{v}_{qp} = \vec{v}_p$. The term $\vec{R}_{pq}$ represents the interphase momentum

exchange, which models the drag force between the phases. This force depends on friction, pressure, cohesion, and other effects, and is subject to the conditions $\vec{R}_{pq} = -\vec{R}_{qp}$, meaning the force between phases is equal and opposite, and $\vec{R}_{qq} = 0$, indicating no self-interaction within a single phase. The interphase interaction term is modeled as:

$$\sum_{p=1}^{n} \vec{R}_{pq} = \sum_{p=1}^{n} K_{pq}(\vec{v}_p - \vec{v}_q) \tag{5.9}$$

Here, K_{pq} is the interphase momentum exchange coefficient, which represents the drag coefficient between phases p and q. This interaction term simplifies the momentum exchange by assuming it is proportional to the velocity difference between the phases. Additional body forces, such as lift ($\vec{F}_{\text{lift},q}$), virtual mass ($\vec{F}_{\text{vm},q}$), and turbulent dispersion ($\vec{F}_{\text{td},q}$), complete the right-hand side of the equation 5.8. For the humid air phase, the momentum equation remains in its general form, capturing the evolution of momentum under the influence of pressure, gravity, and drag forces exerted by the liquid water phase. For liquid water, since it is stationary ($\vec{v}_{\text{lw}} = 0$), its momentum equation reduces to a simpler balance. The simplified momentum equation for liquid water is:

$$0 = -\alpha_{\text{lw}}\nabla p + \alpha_{\text{lw}}\rho_{\text{lw}}\vec{g} + K_{\text{ha}\to\text{lw}}(\vec{v}_{\text{ha}}) + \left(\vec{F}_{\text{lift,lw}} + \vec{F}_{\text{wl,lw}} + \vec{F}_{\text{vm,lw}} + \vec{F}_{\text{td,lw}}\right) \tag{5.10}$$

5.1.4 Conservation of Energy

The conservation of energy within the Eulerian multiphase model plays a crucial role in capturing the heat transfer and phase change processes, which are essential for simulating drying in biomass. The general form of the energy conservation equation for a phase q is expressed as [22]:

$$\begin{aligned}\frac{\partial}{\partial t}\left(\alpha_q\rho_q\left(e_q + \frac{\vec{v}_q^2}{2}\right)\right) + \nabla\cdot\left(\alpha_q\rho_q\vec{v}_q\left(h_q + \frac{\vec{v}_q^2}{2}\right)\right) &= \sum_{p=1}^{n}\left(Q_{pq} + \dot{m}_{pq}h_{pq} - \dot{m}_{qp}h_{qp}\right) \\ &+ \nabla\cdot\left(\alpha_q k_{eff,q}\nabla T_q - \sum_j h_{j,q}\vec{J}_{j,q} + \tau_{eff,q}\cdot\vec{v}_q\right) + p\frac{\partial\alpha_q}{\partial t} + S_q\end{aligned} \tag{5.11}$$

In this equation e_q is the specific internal energy of the phase, the term h_q refers to the specific enthalpy of phase q, which includes the contribution of kinetic energy, represented by $\frac{\vec{v}_q^2}{2}$. The left-hand side of the equation captures the time-dependent change in energy, while the right-hand side represents the different modes of energy transport and exchange. The term $\nabla\cdot(\alpha_q k_{eff,q}\nabla T_q)$ represents the diffusion of heat through the phase, with $k_{eff,q}$ as the effective thermal conductivity. The contribution $\sum_j h_{j,q}\vec{J}_{j,q}$ accounts for the energy transported by the diffusive flux of

species j within phase q. The term $\tau_{eff,q} \cdot \vec{v}_q$ describes the viscous dissipation in phase q due to internal stresses. Energy exchange between phases is captured by the summation over p, which includes several key terms. First, Q_{pq} represents the heat exchange between phases p and q. The term $\dot{m}_{pq}h_{pq}$ describes the heat related to the mass transfer from phase p to phase q, with h_{pq} representing the associated enthalpy (for instance, water evaporating into air). On the other hand, the term $\dot{m}_{qp}h_{qp}$ accounts for the reverse mass transfer (for instance, water condensation). The source term S_q accounts for any external sources or sinks of energy, such as heat generated by chemical reactions or introduced by radiation.

5.1.5 Heat Transfer Coefficient

In multiphase simulations, particularly those involving phase changes like evaporation during the drying of biomass, the heat transfer coefficient plays a crucial role in determining how heat moves between phases. One available and widely used model for estimating the heat transfer coefficient in the Eulerian systems, such as the interaction between humid air and water vapor, is the Ranz-Marshall correlation [21]. This correlation, applicable to systems where small particles (such as liquid droplets or solid particles) interact with a surrounding fluid, computes the heat transfer coefficient h_{pq} between phases p and q as a function of the *Nusselt number* (Nu_p), the *Reynolds number* (Re_p), and the *Prandtl number* (Pr) [22]. The *Nusselt number* relates the convective heat transfer to the conductive heat transfer within the system, while the *Reynolds number* quantifies the flow regime (laminar or turbulent) around the particle, and the *Prandtl number* gives the relationship between momentum and thermal diffusivity. The heat transfer coefficient for two phases is defined as:

$$h_{pq} = \frac{k_q Nu_p}{d_p} \tag{5.12}$$

where h_{pq} $(= h_{qp})$ is the volumetric heat transfer coefficient between phase p and phase q, k_q is the thermal conductivity of phase q, d_p is the diameter of phase p particles (or bubbles, depending on the system). The Nu_p is computed using the *Ranz-Marshall correlation* as follows:

$$Nu_p = 2.0 + 0.6 Re_p^{1/2} Pr^{1/3} \tag{5.13}$$

where Re_p is the Reynolds number for phase p, and Pr is the Prandtl number of the q-th phase. The Reynolds number is based on the diameter of the particles and the relative velocity between the phases. The Prandtl number for phase q is defined as:

$$Pr = \frac{c_{p,q}\mu_q}{k_q} \tag{5.14}$$

where $c_{p,q}$ is the specific heat at constant pressure for phase q, μ_q is the dynamic viscosity of phase q.

In the context of biomass drying, this model is used to calculate the heat transfer between the liquid water phase and the humid air phase. The *Ranz-Marshall* model is particularly suitable for this situation as it applies to heat transfer between dispersed systems, such as water droplets within an air stream, which is analogous to water evaporation in porous biomass. The volumetric rate of energy transfer between phases p (e.g., liquid water) and q (e.g., humid air) can be expressed as:

$$Q_{pq} = h_{pq}A_i(T_p - T_q) \tag{5.15}$$

where Q_{pq} is the heat transferred from phase p to phase q, A_i is the interfacial area between phases p and q, it represents the area over which the liquid water interacts with the humid air. T_p and T_q are the temperatures of phases p and q, respectively, the difference between the two phases, $(T_p - T_q)$, plays a significant role in determining the rate of evaporation, as a larger temperature difference accelerates the phase change.

5.2 Evaporation condensation - Lee model

The Lee model is a mechanistic approach used to simulate interphase mass transfer between liquid and vapor phases during processes such as evaporation and condensation. It provides a numerical solution to handle phase change phenomena where mass is transferred between two phases based on the local conditions. The model simplifies the complex physics of phase change by applying a user-defined coefficient to determine the rate of mass transfer [22] [23]. Indeed, the Lee model solves the conservation equations (2 for continuity, 4 for momentum, and 2 for energy) along with the necessary constitutive correlations. As it has been expressed previously, in 5.5 and 5.6, rates for mass exchange between phases are defined. These rates inside the Fluent simulation are expressed in units of kg/m^3s. The rate of mass transfer with the use of the Lee model is driven by the temperature difference between the phases, where mass transfer occurs from liquid to vapor if the local temperature exceeds the saturation temperature (T_{sat}) and from vapor to liquid if the temperature is below the saturation temperature. These temperature regimes define the following mass transfer conditions:

- If $T_{lw} > T_{\text{sat}}$ (evaporation):

$$\dot{m}_{\text{lw}\to\text{ha}} = \text{coeff} \cdot \alpha_{lw}\rho_{lw}\frac{(T_{lw} - T_{\text{sat}})}{T_{\text{sat}}} \tag{5.16}$$

- If $T_{ha} < T_{\text{sat}}$ (condensation):

$$\dot{m}_{\text{ha}\to\text{lw}} = \text{coeff} \cdot \alpha_{wv}\rho_{wv}\frac{(T_{\text{sat}} - T_{ha})}{T_{\text{sat}}} \tag{5.17}$$

A critical aspect of the Lee model is the fine-tuning of the "coeff" parameter, which acts as a relaxation factor. This user-defined coefficient directly controls the rate at which phase change occurs, influencing how quickly the system responds to deviations in temperature. It is important to note that the coefficient ("coeff") can vary significantly between evaporation and condensation processes. In fact, the parameter might differ between the two, being represented as $coeff_e$ for evaporation and $coeff_c$ for condensation, respectively. This distinction is necessary due to the differing physical dynamics in each phase change process. If $coeff_e$ and $coeff_c$ are set too low, the mass transfer may be delayed, leading to underestimation of the evaporation or condensation rate. Conversely, if set too high, the phase change may be exaggerated, resulting in non-physical behaviors. Therefore, careful adjustment and calibration of these coefficients are necessary to achieve a balance between numerical stability and the physical realism of the simulation. The Lee model requires the saturation temperature, T_{sat}, as an input. However, in reality, T_{sat} is not constant; it varies with pressure, following the Clausius-Clapeyron equation:

$$\frac{dP}{dT} = \frac{L}{T(v_v - v_l)} \tag{5.18}$$

where v_v and v_l are the inverse of the densities of the vapor and liquid phases (volume per unit mass), respectively. L represents the latent heat (in J/kg).

5.3 Porous zone

In the simulation, the woodchips are modeled as a porous medium within the control volume, not only to account for the intrinsic porosity of the wood itself but primarily to simulate the air gaps and void spaces between individual woodchips. Given that the material is loosely packed, air can flow through these voids, resulting in substantial interaction between the phases. To capture this behavior in ANSYS Fluent, the porous media model is applied, treating the woodchip bed as a porous zone [19]. In Fluent, the Superficial Velocity Porous Formulation is utilized to model the airflow through the woodchip bed. This formulation calculates the superficial velocity based on the volumetric flow rate in the porous region. The superficial velocity represents the bulk flow of the air, considering the porosity of the region, and assumes that the flow velocity remains consistent within and outside the porous medium. Although this method does not capture the local velocity variations within the voids between woodchips, it offers a reasonable approximation

of the bulk flow through the porous structure. While this simplification may overlook some fine-scale details, it effectively represents the global pressure drop and flow characteristics of the system. An important aspect of the simulation is the treatment of the wood's physical presence through the concept of porosity. Rather than explicitly modeling the wood's structure, its influence on the system is incorporated by adjusting the porosity parameter. In ANSYS Fluent, porosity is defined as follows:

$$\varepsilon = \frac{V_{available}}{V_{tot}} \tag{5.19}$$

where the $V_{available}$ is the volume that humid air and liquid water are free to occupy, while V_{tot} is the total control volume. With the introduction of porosity, the volume fraction definitions differ from those described in 5.1.1. Specifically, the volume referenced by the volume fractions is no longer the total meshgrid volume but the volume available to the gas and liquid phases. Therefore, the equation can be rewritten as follows, here expressed for the humid air phase:

$$\alpha_{ha} = \frac{V_{ha}}{\varepsilon\, V_{tot}} = \frac{V_{ha}}{V_{available}} \tag{5.20}$$

Additionally, the distribution of volumes within the control volume can be explained using the following equation:

$$V_{tot} = V_w + V_{available} = (1-\varepsilon)\, V_{tot} + \varepsilon\, V_{tot}(\alpha_{lw} + \alpha_{ha}) \tag{5.21}$$

where V_w is the volume of the wood.

For what concern the dynamic of the flow through the porous medium, it is modeled by adding a momentum source term to the standard fluid flow equations. This source term accounts for both viscous losses (described by Darcy's law) and inertial losses, which contribute to the overall pressure drop across the porous medium. The source term, S_i, representing the impact of the porous structure on the i-th momentum equation (where $i = x, y, z$), is defined as:

$$S_i = -\left(\mu \frac{v_i}{\alpha} + C_2 \frac{1}{2} \rho |v| v_i\right) \tag{5.22}$$

where S_i is the source term for the i-th momentum equation (x, y, or z direction), μ is the dynamic viscosity of the fluid, α is the permeability of the porous medium (a measure of how easily fluid can pass through the porous structure), v_i is the velocity in the i-th direction, C_2 is the inertial resistance coefficient, accounting for the contribution of inertia to the pressure drop, ρ is the fluid density, and $|v|$ is the magnitude of the fluid velocity. Locally, a bed of irregularly shaped wood particles results in non-uniformly distributed bed porosities. Furthermore, the viscous and inertial resistance coefficients ($\frac{1}{\alpha}$ and C_2) vary depending on the flow direction. In

Fluent, the porous zone is modeled as homogeneous in terms of porosity, with a constant value across space and time. However, in reality, the material's effects on the flow differ based on the direction. Fluent allows for different values of $\frac{1}{\alpha}$ and C_2 to be specified for each direction: x, y, or z [22]. Based on the results from M. Mayerhofer et al. (2010) [24], the values presented in Table 5.1 will be used for the Fluent simulations in this study. It is important to note that the y-direction

Viscous and Inertial resistance	
$(1/\alpha)_x$	3×10^7 $1/m^2$
$(1/\alpha)_y$	5×10^7 $1/m^2$
$(1/\alpha)_z$	3×10^7 $1/m^2$
$(C_2)_x$	1500 $1/m$
$(C_2)_y$	4000 $1/m$
$(C_2)_z$	1500 $1/m$

Table 5.1: Value of Viscous and Inertial resistance coefficients based on the direction (x, y, or z)

always refers to the direction perpendicular to the ground, which is also used to represent the height of the woodchip pile. In the case of a 2D representation, the z-coordinate is not considered.

5.4 Boundary conditions

In this simulation, boundary conditions are set to define the behavior of the airflow and water phase entering and exiting the computational domain, crucial for modeling the drying process of woodchips accurately. The boundary conditions employed in ANSYS Fluent control the flow rates, temperature, and species concentrations at the inlet and outlet other than the interaction of the fluids with the walls [22].

5.4.1 Inlet Boundary Condition

A velocity-inlet boundary condition is applied at the inlet, with Fluent allowing the user to specify the velocity, temperature, and species concentrations for both the gas and liquid phases entering the domain. The velocity-inlet condition is chosen because it ensures that the flow is driven by a prescribed velocity rather than pressure. This is especially crucial in the case of forced convection (such as when a fan is present), where the airflow is externally driven. The boundary condition

is configured as follows: the velocity can be specified as a constant value or as a profile, depending on the complexity of the flow entering the domain. In this model, the velocity has been assumed to be constant in the inlet area's. Fluent allows the specification of different species concentrations or volume fractions at the inlet. In this case, the inlet is defined for humid air, while the liquid water is set to a null value, indicating the absence of liquid water entering the system. The inlet temperature is specified to provide the thermal boundary conditions necessary for calculating heat transfer between the incoming air and the porous medium. Fluent uses this temperature as a driving factor in the heat exchange and evaporation process. Indeed, it has a huge influence on the evaporation rate and drying time of the process. [25]

5.4.2 Outlet Boundary Condition

At the outlet, a pressure-outlet boundary condition was defined to allow the fluid to exit the computational domain freely. This condition was selected because it maintains a constant pressure at the outlet while letting the flow variables adjust based on the simulation's internal dynamics. The pressure-outlet boundary condition is particularly suitable for systems where the outflow is pressure-driven, ensuring that the boundary does not artificially constrain the velocity or temperature at the outlet. The outlet is set to a gauge pressure of 0 Pa, representing ambient atmospheric pressure. This allows Fluent to compute the outflow based on pressure gradients within the domain, enabling the humid air and evaporated water vapor to exit naturally. In the event of reverse flow, Fluent requires the specification of backflow conditions for species concentration and temperature. The backflow temperature can be set to the ambient one, and the backflow volume fraction of liquid water is defined as zero to reflect the assumption that no liquid water is expected to re-enter the domain from the outlet. In this case, since a level of free space (humid air) is left upon the porous medium, backflow is not expected in this type of simulation. Indeed, if it does occur, it could be typically an indication of an error.

5.4.3 Wall Boundary Conditions

In Fluent, there are several options for modeling wall boundary conditions. In this study, the walls are considered impermeable, meaning that no mass flow can enter or exit the system through them, effectively preventing any losses or leakage. From a thermal perspective, the walls are modeled as adiabatic, implying that there is no heat exchange between the inside and outside of the control volume. Regarding the impact of the walls on the fluid dynamics, two main boundary conditions are described here. The first is the "no-slip condition", which enforces a zero velocity

at the wall for the fluid in the immediate layer adjacent to it. This condition accurately represents physical walls where frictional forces cause the fluid to come to a complete stop at the boundary. This feature will be applied in Chapter 6. The second option allows for defining zero shear stress at the fluid-wall interface, which assumes that the walls do not induce any frictional losses on the flow. This is particularly useful in cases involving symmetry or idealized scenarios where wall effects are negligible, and it will be applied in Chapter 7 [19][22].

5.5 Computational Fluid Dynamics aspects

Computational Fluid Dynamics is a branch of fluid mechanics that employs numerical methods to solve and analyze problems involving fluid flows. By solving the constitutive equations governing fluid behavior CFD enables the prediction of various phenomena like fluid flow, heat and mass transfer, and chemical reactions. The strategy of CFD involves transforming the continuous problem domain into a discrete domain by using a grid. Therefore, the fluid region of a flow is divided into a finite set of control volumes. In this way the physical domain is discretized and, in the case of Fluent, a mesh composed by those control volumes is obtained. The governing equations for mass, momentum, and energy are then solved numerically within these control volumes. This process translates the partial differential equations into a system of algebraic equations, which can then be solved iteratively until the solution reaches convergence [26].

5.5.1 Transient Simulation

In transient situations, the simulation aims to capture time-dependent behaviors, meaning that the solution changes at each time step as the system evolves. Convergence in these simulations refers to the state in which the changes in solution variables between successive iterations within a given time step become negligible. In this context, achieving convergence at each time step is essential to ensure the accuracy and reliability of the transient simulation. In transient CFD simulations, the governing equations are solved iteratively for each time step. The solution at each time step must converge before proceeding to the next one. In Fluent, the criteria for convergence are typically defined based on residuals, which measure the difference between the current solution and the solution from the previous iteration. When these residuals fall below a pre-set threshold, the solution for that time step is considered converged [22].

5.5.2 Time Step Size

The choice of the time step is crucial. A time step that is too large may result in significant errors, as the transient effects may not be captured adequately. On the other hand, a very small time step increases the computational cost. The time step must be chosen carefully to balance accuracy and efficiency, ensuring that the simulation remains stable and converges within a reasonable number of iterations. The use of the Courant-Friedrichs-Lewy (CFL) number is usefull to evaluate a feasible timestep [26]. The CFL condition states that the distance (in length) that any information travels within a timestep must be smaller than the distance between mesh elements. In other words, during each time step, information from a given cell or mesh element should propagate only to its immediate neighbors and not extend beyond them. This ensures that the numerical solution progresses in a stable and controlled manner, preventing the violation of physical principles. The CFL is defined as:

$$C = \frac{v\ dt}{dx} \tag{5.23}$$

where C is the CFL number, v is the flow velocity, dt is the time step and dx is the spatial resolution of the mesh (the size of the control volume in the direction of the flow velocity). In this study, a CFL value close to 1 is considered reasonable for most cases. However, for high-speed flows, it may be necessary to reduce the CFL value further, even below 0.5, to ensure stability and accuracy without any issues [19][26].

Chapter 6

Model Validation Through Existing Experimental Data

The paper by Peter Bengtsson [25] focuses on the experimental analysis of low-temperature drying of biomass particles, specifically wood chips and sawdust, to prepare them for a gasification process. This process requires dry biomass as the drying operation is critical and energy-intensive. The study evaluates the effectiveness of using waste heat for drying, a technique that could significantly reduce energy consumption and associated costs.

The primary objective of the study was to examine the influence of various parameters, such as air temperature, air velocity, bed height, and type of wood, on the drying rate, final moisture content, and pressure drop across the drying bed. The early stages of the drying process are characterized by a constant-rate period, followed by a falling-rate period, with the drying zone progressing irregularly through the bed.

This paper is relevant to this work as it allows for a comparison between the previously described model and the experimental results obtained by Bengtsson. Specifically, it is valuable to analyze the model's behavior in terms of the drying rate and the time required to achieve complete drying.

6.1 Experimental setup

The experimental setup includes a fixed bed dryer capable of drying 0.25 m^3 of biomass per batch. Heated air, warmed through an electric heater, is forced from the bottom of the drying chamber, ensuring a controlled drying process. Various sensors monitor the temperature and humidity of the air at the inlet and outlet, as well as the pressure drop across the bed. In Figure 6.1 the scheme of the experimental setup is represented:

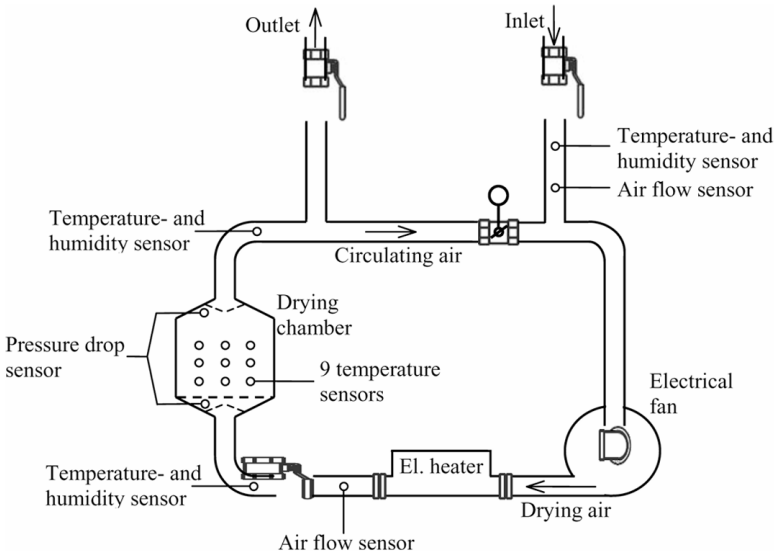

Figure 6.1: Experimental setup of the drying chamber from Bengtsson's paper, illustrating the airflow system, sensor placements and the key components [25]

Three main airflow streams are used in this experiment, each controlled by a valve to shut off the duct when necessary. The first stream, labeled as 'Inlet,' draws air from the outside, with temperature, humidity, and flow rate measurements recorded. The 'Outlet' stream represents the hot, humid air that is released to the outside after passing through the drying chamber. A portion of this flow can be diverted and recirculated back into the system to reduce energy consumption, particularly during the preheating phase of the experiment. The flow rate of the recirculated air is controlled by an electrically operated valve, which adjusts the pressure drop across the line and regulates the amount of air passing through. The inlet air, combined with the recirculated flow, is then pushed through the fan and heated by the electrical heater. Before entering the drying chamber, the air passes through a sensor array that measures the flow rate and thermodynamic properties. A similar process occurs at the outlet of the drying chamber, where the air either exits the system (Outlet stream) or is recirculated back into the system

6.2 Drying chamber modelisation

In the paper [25], the drying chamber used was cylindrical, with a diameter of 0.8 m. However, in the Fluent model, the chamber is recreated as a parallelepiped with a square base to simplify the computational process. The square base has sides measuring 0.71 m, and the chamber was filled to a height of 0.42 m. The inlet and outlet areas were maintained consistent with the original design to preserve the same volume. The change in geometry altered the border effects, but these were considered negligible. This square-based design allowed for the creation of a mesh grid with cubic cells, which significantly reduced computational complexity and enhanced the stability and convergence of the solution.

This square-based design allowed for the creation of a mesh grid with cubic cells, each measuring 0.02 m. This uniform grid ensured an orthogonal quality of 1 for each cell within the control volume, which is usefull to increase the reliability of the simulation results. Additionally, the mesh grid includes 10 cm of cells filled only with humid air both below the inlet and above the outlet. These air-filled cells are strategically placed to smooth the transition between the differing conditions of the input/output and the woodchips, particularly at the beginning of the simulation when the differences are most pronounced. This setup helps prevent abrupt changes in the simulation, enhancing both stability and accuracy. Below, Figure 6.2 is an image of the mesh grid used in the simulation, illustrating the structure of the cubic elements:

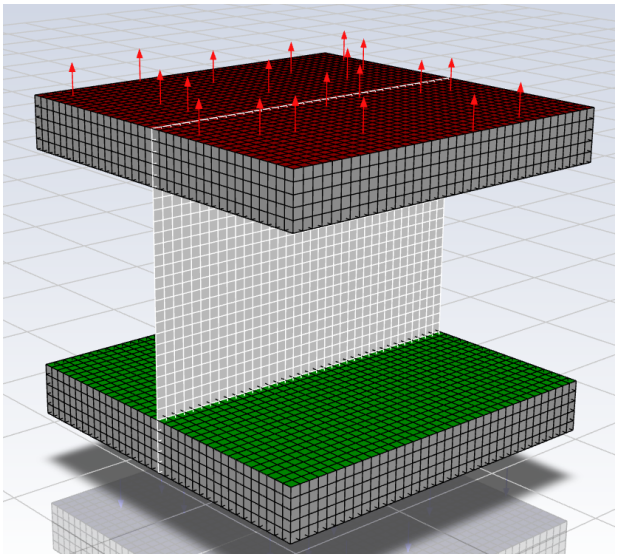

Figure 6.2: Meshgrid of the drying chamber in Fluent with the dx of 2 cm

6.3 Thermodynamic condition of the experiment

Several graphs from the paper provide a comprehensive overview of the initial conditions, illustrating the different variables such as temperature, specific humidity, and other relevant parameters. Those are posted here below to depict the condition used in the experiment:

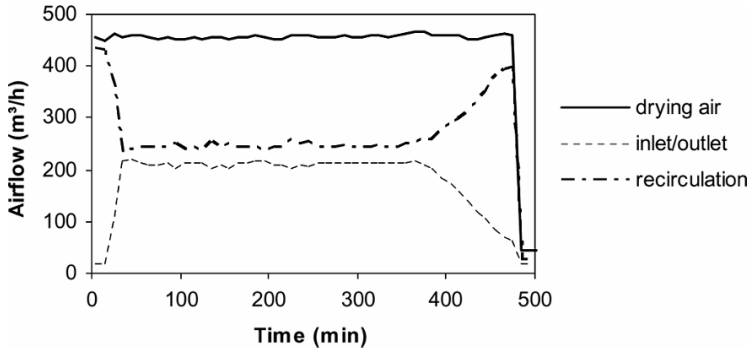

Figure 6.3: Experimental airflow conditions showing the variation over time for drying air, inlet/outlet flow, and recirculation [25]

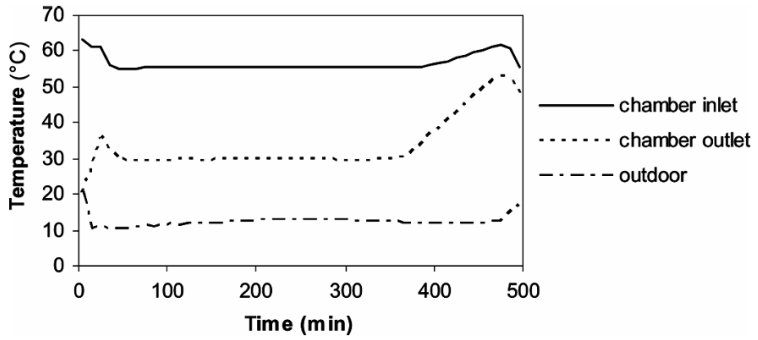

Figure 6.4: Experimental temperature conditions over time, showing the chamber inlet, chamber outlet, and outdoor temperatures [25]

At time $t = 0$ s, the conditions inside the chamber are characterized by the temperature at the outlet reaching the wet bulb temperature. The wet bulb temperature is the temperature at which the air cannot hold any more moisture and is fully saturated. In the context of the drying process, this temperature represents the point where the air has absorbed the maximum amount of moisture

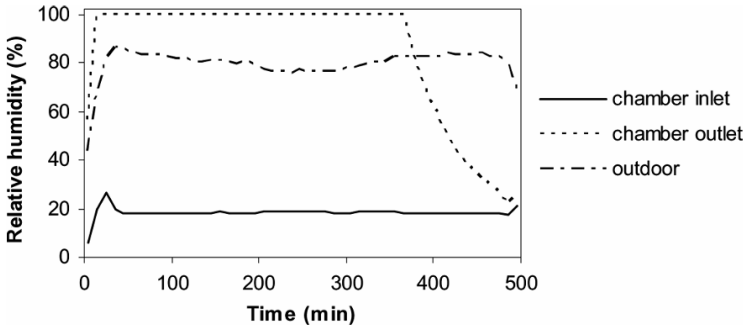

Figure 6.5: Experimental relative humidity conditions over time, illustrating the chamber inlet, chamber outlet, and outdoor humidity levels [25]

from the wet material. This condition indicates that the drying experiment is ready to start and that the pre-heating phase is complete. In the Fluent simulation, the initial conditions are set such that the entire drying chamber has a uniform temperature equal to the wet bulb temperature. This also means that, the relative humidity is maximum and equal to 100 %. This ensures that the simulation reflects the initial state of the experimental drying process, with the air fully saturated and ready to exit from the outlet. The value of moisture content at the start of the simulation is given in the text of the paper and it has been obtained through the analysis of 3 different samples, resulting in an average value of 115 % [25]. Same procedure has been used at the end of the experiment to evaluate the final moisture content that corresponds to an average value of 5.6%. Regarding the velocity at the inlet, it is assumed to be uniform across the entire inlet area. The flow velocity is calculated as the ratio between the volumetric flow rate and the inlet section. The initial condition are listed in Table 6.1 and the condition at the inlet of the drying chamber used in the experiment are resumed in Table 6.2:

Starting condition	
T_0	32 °
RH_0	100 %
MC_0	115 %

Table 6.1: Starting condition of the drying chamber after the preheating period

Inlet condition	
$\dot{V}_{in}$	500 m^3/h
T_{in}	57 °
RH_{in}	20 %

Table 6.2: Inlet condition of the drying chamber during the experiment (preheating phase excluded)

The following one includes the transformation of specific values to make them compatible with Fluent requirements. The relative humidity is converted into absolute humidity, a Fluent-compatible parameter, and moisture content is transformed into a volume ratio of liquid water using Equation 4.5 and Equation 5.20.

Drying chamber initial condition	
T_0	305 K
x_0	22.8 g_{wv}/kg_{air}
ε	0.6
α_{lw}	0.25 m^3/m^3
Drying chamber inlet condition	
u_y	0.25 m/s
T_{in}	330 K
x_{in}	22.1 g_{wv}/kg_{air}

Table 6.3: Simulated condition of the drying chamber inside ANSYS Fluent

6.4 Fluent simulation

The time step for the early stages of the simulation is carefully selected based on the Courant-Friedrichs-Lewy number (CFL, as explained previously in 5.5.2). In order to keep it equal or under the unity, the value of dt is evaluated:

$$dt \leq \frac{dx}{u} = \frac{0.02}{0.25} = 0.08 \tag{6.1}$$

Therefore a dt of 0.05 seconds is chosen to prevent convergence issues, ensuring a smooth and efficient progression of the solution during the initial iterations. Convergence is considered achieved when the residuals of each governing equation (such as energy, continuity, momentum, volume fraction, etc.) are all below 1×10^{-3}.

In the simulation of this experiment, convergence is achieved from the very first timestep, within the maximum number of iterations set to 50. After approximately 40 time steps, convergence is consistently achieved from the first iteration of each new time step. After the convergence is reached constantly for several timestep, the CFL constriction can be slightly relaxed and the *dt* has been carefully and smoothly changed to higher values in order to reduce the total computational cost and the operational time.

6.5 Results comparison

The purpose of this analysis is to compare the experimental results from the paper with those obtained through simulation using the Fluent model. Data from the software have been collected through the creation of datafile ASCII based every 30 seconds during the simulation. The ASCII files have been analyzed through a Python script and graphical and numerical results have been obtained. Several parameters can be examined to assess the accuracy of the model, with one of the most important being the total time required to achieve the same level of drying. In the experiment the process has been stopped at 482 minutes, when the relative humidity at the outlet of the drying chamber dropped below 25 %. In the simulation results, analysis of the data using the Python script shows that the 25 % RH at the outlet is reached at approximately 440 minutes. The difference between the experimental and simulation times is significant. However, as mentioned in the paper, potential lagging errors in the humidity sensor may have led to discrepancies in the overall results. Assuming the 482-minute experimental value as correct, the relative error is 8.7 %.

Another key parameter is the amount of water evaporated during the experimental process, which was condensed, collected, and weighed at the end, totaling 31.4 kg. This value was also estimated through a mass balance using data from the humidity sensors, yielding a result of 35.4 kg, indicating a difference of 12.7 %. In the Fluent simulation, this value is not treated as a result, as the amount of water is predefined in the initial conditions.

In the results presented in the paper, the graph shown in Figure 6.6 illustrates the drying ratio (r), which represents the amount of water evaporated during the drying process over a specific period. It was calculated based on a mass balance using data from the two series of sensors located at the inlet and outlet of the drying chamber. In Fluent, the drying ratio was computed in the same way, keeping in mind that no liquid water entered or exited the drying chamber. The drying ratio can be determined using the following Equation 6.2:

$$r = m_{outlet} - m_{inlet} = (x_{outlet} - x_{inlet})\ u_{ha}\ A_{chamber}\ \rho_{air} \tag{6.2}$$

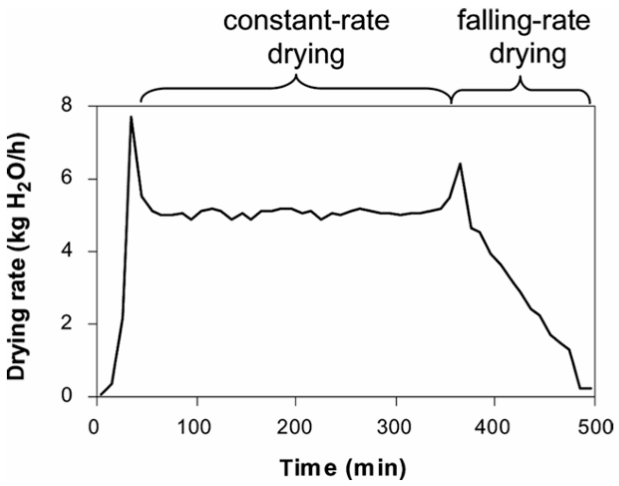

Figure 6.6: Drying rate over time from Bengtsson's paper, showing the transition from the constant-rate drying phase to the falling-rate drying phase [25]

where x represents the water vapour content in the humid air, u_{ha} is the velocity in the y direction, ρ_{air} is the density of the dry air and $A_{chamber}$ is the cross section area of the drying chamber. The obtained value is measured in kg/s.

The graph in Figure 6.6 can be divided into three main phases. In the first phase, during the initial minutes of the experiment, a sharp increase in the drying ratio is observed, marking an initial transient period. Following this, the system enters a second phase known as the 'constant-rate drying' period, where the drying ratio remains steady. During this phase, the wood, exposed to the incoming hot air, releases sufficient moisture, causing the outgoing air to be saturated with humidity (relative humidity at 100 %) as it exits the chamber. This period continues until around 370 minutes. After this point, the third phase, known as the 'falling-rate drying,' begins. Here, the value of r decreases significantly, as the wood is no longer able to release enough moisture to saturate the air. This final phase ends at 482 minutes when the experiment is concluded. Consequently, the paper suggests that systemic errors may be present in the use and measurement of the humidity sensors. Furthermore, the author notes in the conclusion that the air in this drying test was heated above the wet-bulb temperature of the drying temperature, which led to an unrealistically high drying rate at the beginning of the test. Additionally, the paper mentions an unexpected small peak at the start of the falling-rate drying period, indicating an increasing drying rate, likely due to lag in the humidity sensor [25].

To more effectively compare the drying ratio behavior between the experiment and the simulation, the two resulting graphs are overlaid in Figure 6.7. For consistency, the Fluent results were converted to kg/h by multiplying by 3600, and

the experimental curve was reproduced graphically using Python.

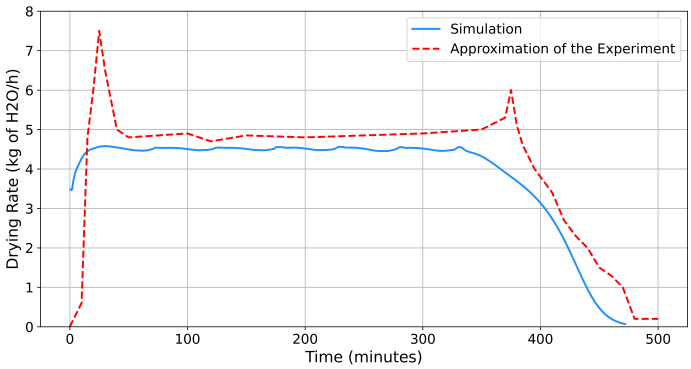

Figure 6.7: Comparison between the drying rates: the red one obtained from the humidity sensors in the paper and the blue one obtained with the Fluent simulation

The integral of the drying ratio curve represents the total amount of water evaporated within the chamber. The red dotted line is the graphical reproduction of the experimental data. While slightly imprecise, its integral gives an evaporated water value of 35.4 kg, closely aligning with the value reported through the use of humidity sensors in the paper. For the blue line, representing the Fluent simulation results, the integral was computed using a Python function, yielding 31.2 kg. This value is very close to the experimentally weighted water of 31.4 kg, with a margin of error within 1 %.

To better evaluate the model results, other two key values are monitored: temperature and relative humidity at both the inlet and outlet. These two variables are shown in Figure 6.8 and 6.9.

6.6 Conclusions

Based on the various results discussed in the previous section, it can be concluded that the model performs relatively well when compared to the experimental data. It is important to note that these results are influenced by the fact that the material used in the experiment was sawdust, not woodchips, as is the case in the study presented in Chapter 3. The main differences between the experimental data and the model lie in the initial transient phase, which in the Fluent model is much slower and lacks a well-defined peak. Additionally, there is a secondary peak at the beginning of the "falling-rate period," which can be disregarded due to the lagging of the humidity sensors as explained in the reference paper. As for the behavior of temperature and relative humidity, it can be stated that the model aligns well with

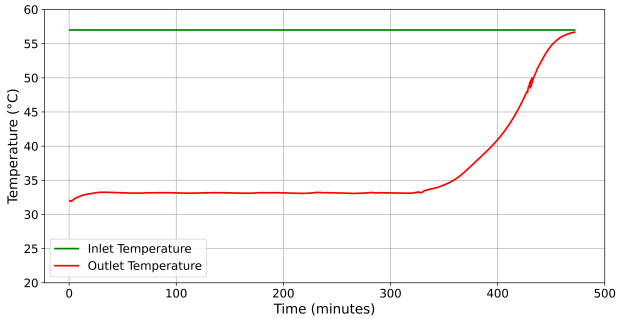

Figure 6.8: Simulation of temperature over time in the Fluent model, showing the inlet temperature remaining constant and the outlet temperature gradually increasing before a sharp rise near the end of the process

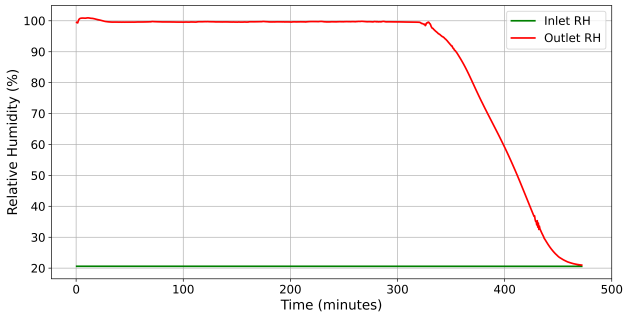

Figure 6.9: Simulation of relative humidity over time in the Fluent model, illustrating the constant inlet humidity and the decreasing outlet humidity as the drying process progresses, particularly after 300 minutes

the experimental data, though in real scenarios it is naturally much more difficult to maintain completely constant inlet conditions. It is also worth noting that in the early moments of the simulation, the relative humidity in the Fluent model exceeds 100 %, a result that is not physically accurate, as water vapor under those conditions should have condensed more rapidly than predicted by the model.

Despite these discrepancies, the close match in drying times and the close amount of evaporated water suggests that the model is suitable for the purposes of this case study.

Chapter 7

Fluent application

In this final chapter, the application of ANSYS Fluent to the case study is presented, building on the theoretical foundation and methodology outlined in the previous chapters. The simulation focuses on modeling the drying process in a woodchip pile, taking into account the airflow dynamics and heat transfer mechanisms described earlier. The setup of the simulation involves defining the meshgrid, material properties, boundary conditions, and initial conditions specific to the case study. These parameters have been carefully tailored to reflect the real-world operating conditions of the system. The chapter also details limitations of the simulation, and the adjustments necessary to fit within the computational resources available. This practical application of Fluent provides a basis for analyzing the system's behavior under various conditions, offering insights into the drying phenomena and system performance.

7.1 Meshgrid

A full 3D simulation covering the entire length of the channels would require a professional license, as this would remove any restrictions on the maximum number of nodes and cells available in the mesh grid (in this work, a Student license is used).

To address this limitation, only a section of the total length is analyzed, with the assumption that the drying behavior is consistent along the entire length of the plant. This section is considered to have an infinitesimally small thickness, which in Fluent is represented by a 2D simulation. The section includes the woodchip pile, the five channels beneath it, and a thin layer of air above. The cement walls on the sides are assumed to have minimal influence on the drying process due to their significant thickness, which reduces thermal losses and has a relatively low impact on airflow. Naturally, this is an approximation, and in reality, the biomass

near the walls may remain wetter than the rest. Additionally, the section can be simplified and reduced due to the presence of symmetries and periodicities. Each channel has identical dimensions and exerts the same influence on the woodchips directly above it. This concept is illustrated in Figure 7.1, where the boundary of the influence of a single channel in the actual system is outlined in green.

Figure 7.1: Overlay of the woodchip pile and meshgrid dimensions on the real case study plant. The green highlight shows the section modeled in the simulation

To reduce computational complexity, only a single channel is modeled in the Fluent simulation, taking advantage of its vertical symmetry. As highlighted in red in Figure 7.1, a symmetry axis is present, allowing the channel to be divided vertically due to its symmetrical properties. This approach enables the generation of a mesh grid that accurately represents half of the channel while preserving the accuracy of the airflow and drying behavior simulations. Three distinct zones are defined: the inlet zone, where a portion of the channel is represented to minimize instability at the interface between the incoming air and the porous material; the porous zone, where the woodchips are located; and the outlet zone, which serves as a transition between the external environment (air) and the porous material. This transition helps stabilize the boundary condition cells and reduces numerical instabilities.

7.2 Materials parameters

The materials and chemical compounds defined in Fluent for this case study are categorized into three groups: woodchips, humid air, and liquid water, as previously described. For air and water, the thermophysical and mechanical properties remain unchanged from the default values provided by Fluent [19]. For the woodchips, the "Wood" material from the software's database serves as a reference, but both the specific heat capacity and density are modified. The values used in this simulation are derived from the explanations provided in Chapter 4. For the temperature range between $5°C$ and $50°C$, the formula in Equation 4.7 calculates a specific heat capacity (c_p) between 1.18 and 1.35 $kJ/kg\,K$. Based on literature and considering the impact of the water content within the wood particles, along with the energy required to break the wood-water bonds, a constant c_p value of 1.25 $kJ/kg\,K$ is applied in the simulation [12]. Regarding the density, an average value is selected from those found in the literature, as outlined in Section 4.2, resulting in a final value of $1300 : kg/m^3$ [14]. An additional key parameter for defining the structure of the woodchip pile and determining its porosity is the bulk density. Based on the evaluation by Amato et al. (2020) [16], a bulk density of 245 kg/m^3 is selected. The bed porosity, ε, represents the fraction of the bed volume occupied by air. For agricultural or woody biomass in packed beds, the porosity typically ranges from 0.6 to 0.9. For this application, using Equation 4.4, a porosity value of approximately 0.8 is obtained.

In the following Table the different parameters adopted for the simulation of woodchips are resumed:

Material Paraameters	
C_p	1.25 $kJ/kg\,K$
ρ_w	1300 kg/m^3
BD_w	245 kg/m^3
ε	0.8

Table 7.1: Values adopted in the Fluent software to represent the woodchips

7.3 Boundary Conditions

As discussed in Chapter 5, the boundary conditions relevant to this study include a fixed inlet velocity, a constant outlet pressure, and wall conditions. These conditions are essential for accurately modeling the airflow and the interaction with the surrounding environment.

7.3.1 Inlet Velocity

To compute the velocity at the inlet of the control volume of the meshgrid described in 7.1, several assumptions are necessary. It is assumed that no mass flow rate losses occur along the channels, an even distribution of flow rate at every point within the channels, and no pressure losses in the ducts between the fan and the point of contact with the wood. Additionally, we consider that the grids separating the wood from the channels do not introduce significant pressure drops.

Based on the previous assumptions and constraints, the volume flow rate through each channel can be calculated as follows:

$$\dot{V}_{channel} = \frac{\dot{V}_{tot}}{N_{channel}} = \frac{5.5\ \mathrm{m}^3/\mathrm{s}}{5} = 1.1\ \mathrm{m}^3/\mathrm{s} \tag{7.1}$$

The number of channels $N_{channel}$ can be obtained from the technical drawings provided in Chapter 3, while the total flow rate is derived from Table 3.1, which is based on the technical specifications of the fan. The air velocity at the inlet of the meshgrid can then be determined using the equation 7.2:

$$v_y = \frac{\dot{V}_{channel}}{A_{inlet}} = \frac{\dot{V}_{channel}}{L * W} = \frac{1.1\ \mathrm{m}^3/\mathrm{s}}{24\ \mathrm{m} * 0.3\ \mathrm{m}} = 0.15\ \mathrm{m/s} \tag{7.2}$$

Here, A_{inlet} represents the inlet area of the channels, which can alternatively be described as the surface area of the grids or the top area of the channels. This area is calculated by multiplying the length and width of a single channel.

7.3.2 Wall boundary condition

The walls of the meshgrid in this case study are treated as thermally adiabatic, meaning no heat transfer occurs through them, ensuring that all thermal energy is retained within the system. From a fluid dynamics standpoint, the walls are defined with zero influence on the flow, characterized by a shear stress value of zero. Their primary role is to contain the humid air flow and liquid water, acting as impermeable barriers and preventing any form of leakage or energy loss from the system.

7.3.3 Outlet condition

For the outlet condition of this study, the gauge pressure is set to 0 Pa in the Fluent simulation, meaning that the outlet pressure is equal to the ambient atmospheric pressure. This ensures that the airflow exits the meshgrid under the same pressure conditions as the surrounding environment, maintaining a realistic simulation of the outflow behavior.

7.4 Initial Condition

In this study, it is assumed that both the woodchips and the surrounding air are at the same conditions as the outside air when the simulation starts. Temperature is set at $5°C$ and relative humidity is constant at 60%, these two values are based on typical average year winter conditions in Belgium [27]. These parameters are specified using the patch function in Fluent, allowing for different values to be assigned across the three zones previously defined.

7.4.1 Volume Fraction of Water

The moisture content data provided by the company Intradel, in accordance with the EN 14774 standard, outline the initial and final moisture content of the available wood biomass on a dry basis [28]. These values are presented in the table below:

Moisture Content	
Initial MC	$70\% \pm 10\%\ kg_w/kg_{db}$
Final MC	$30\% \pm 5\%\ kg_w/kg_{db}$

Table 7.2: Moisture content on a dry basis of woody biomass according to EN 14774.

Fluent does not permit the direct input of moisture content into the simulation. Instead, it requires the specification of the volume fraction (α_{lw}) of liquid water as an initial condition at $t = 0s$. To meet this requirement, the following formula is applied, which is derived from Equation 4.5 and the definition of volume fraction (5.1.1):

$$\alpha_{lw} = \frac{V_{lw}}{V_{available}} = \frac{\rho_w}{\rho_{lw}} \frac{V_{tot}}{\varepsilon\, V_{tot}} (1-\varepsilon) \frac{MC_0 - MC_{final}}{100} \tag{7.3}$$

In this context, $V_{available}$ represents the volume that can be occupied by liquid water and humid air, excluding the volume taken up by the wood itself, as described in section 5.3. Therefore, the obtained value of α_{lw} is 0.13.

7.5 Addressing Computational Limitations: Reductions and Adjustments

Once the model is implemented in Fluent, the velocity field is analyzed, with the results separated into the velocity components along the X and Y directions, with particular attention given to the first meter above the inlet, as shown in Figure 7.2. This initial analysis suggests that the inlet significantly affects the velocity profile up to approximately 80 cm. Beyond this point, the airflow becomes increasingly linear, leading to an expected uniform moisture loss behavior in the woodchips.

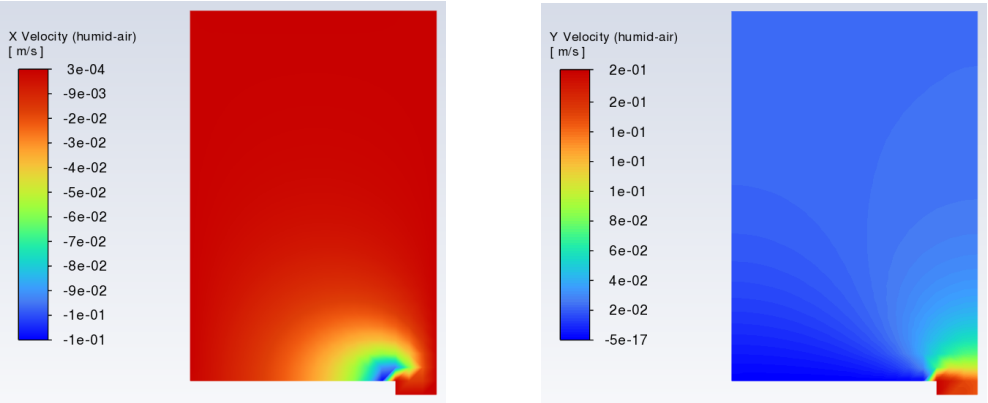

Figure 7.2: Left side: velocity of humid air along X axis; Right side: velocity of humid air along Y axis

Given the initial and inlet conditions, the drying rate can be estimated under theoretical assumptions. Assuming that the air exiting the outlet is fully saturated, the drying rate during the constant drying rate phase can be calculated using Equation 6.2 provided in Chapter 6, with appropriate adjustments for area and velocity the formula trasforms into:

$$r = (x_{outlet} - x_{inlet}) \;\; u_{inlet} \;\; A_{inlet} \;\; \rho_{air} \tag{7.4}$$

Therefore, under the conditions expressed in Table 3.1 and Table 7.3 the drying rate during the constant phase is estimated at approximately 0.73 kg/h. Considering the large volume of the woodchip pile, its significant height, and the substantial reduction in moisture content targeted, the total amount of water to be evaporated is around 420 kg. As a consequence, given these constant conditions, the estimated drying time is expected to extend beyond 24 days.

However, the simulation is further constrained by the fineness of the meshgrid and the Courant–Friedrichs–Lewy number, which limits the time step (dt) to

Theoretical Drying condition	
T	5 °
x_{inlet}	3.2 g_{wv}/kg_{air}
T	15 °
x_{outlet}	10.7 g_{wv}/kg_{air}

Table 7.3: Theoretical drying conditions used to estimate the drying rate, based on inlet and outlet specific humidity (x) and temperature (T) data

approximately 0.5 seconds. The computational speed achieved by the machine used in this study was approximately 80 timesteps per minute, as observed in the simulation discussed in Chapter 6. Given these constraints, a full simulation would be impractical within the available time and resources. Moreover, performing such a simulation would require a high-performance computing system, which exceeds the capabilities available for this study.

To overcome these computational challenges, two key modifications are introduced:

1. **Reduction in Moisture Content Difference (ΔMC)**: The moisture content difference is reduced to 1%, significantly decreasing the amount of water to be evaporated. This adjustment reduce the evaporated water mass by a factor of 40, resulting in a new α_{lw} value of approximately 0.00325.

2. **Reduction in Woodchip Pile Height**: The height of the woodchip pile is reduced to one meter. This allow the simulation to capture the velocity and pressure fields while maintaining the influence of inlet and outlet conditions. Although simplified, this model still provides an accurate representation of the drying process occurring in the case study, offering a reliable reference for future full-scale simulations.

Table 7.4 concludes this section by summarizing all the initial values used in the simulation, along with the new assumptions introduced. The values are organized according to the respective zones where they are applied. As for the inlet conditions, they remain unaffected by the reductions discussed in this section.

Channel zone	
T_{ha}	278 K
x	3.2 g_{wv}/kg_{air}
Porous zone	
T_{ha} and T_{lw}	278 K
x	3.2 g_{wv}/kg_{air}
α_{lw}	3.25×10^{-3} m^3_{lw}/m^3
Outlet zone	
T_{ha}	278 K
x	3.2 g_{wv}/kg_{air}
P	101325 Pa

Table 7.4: Table with the Initial Condition values used in the Fluent simulation

7.5.1 Updated Mesh Grid

Following the previous adjustments, a new mesh grid is created, as shown in Figure 7.3, with the dimensions updated accordingly. By analyzing the mesh grid using the Check Case function [19], it is obtained that the orthogonal quality is 1 for 100% of the cells, ensuring high mesh quality. As shown in Figure 7.3, a grid spacing (dx) of 0.05 cm is selected to ensure sufficient mesh refinement without excessively increase the CFL number.

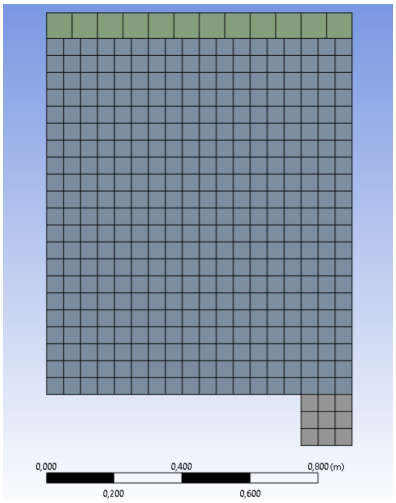

Figure 7.3: Simulation

7.6 Time-step size and CFL number

The time step for the early stages of the simulation is selected based on the CFL number as seen previously in Section 5.5.2). In order to keep it under the unity, the value of dt is evaluated:

$$dt \leq \frac{dx}{u} = \frac{0.05}{0.15} = 0.33 \tag{7.5}$$

A time step (dt) of 0.1 seconds is chosen to prevent numerical instabilities and ensure the accurate initialization of the first timesteps in the simulation. In this application, convergence is achieved from the very first timestep, within the maximum number of 50 iterations. After consistent convergence over several timesteps, the CFL restriction can be gradually relaxed, allowing dt to be smoothly increased, with a maximum value of 1 second applied during the constant drying phase of the simulation.

7.7 Results

The results obtained from Fluent are saved every 30 seconds in ASCII files and are subsequently analyzed using Python scripts. The key parameters are monitored directly within Fluent using the Contour and Report functions.

The first value that can be evaluated is the total time necessary to complete the drying process. As shown in the following Figures 7.4 7.5 7.6, the duration is about 10 hours. This value is determined when the Outlet relative Humidity reaches the same level as the Inlet Relative Humidity.

The primary thermodynamic and physical variables analyzed include the temperature, the relative humidity of the air, the drying rate, the mass of water present in the wood zone, and the mass transfer occurring between the water phases within the same zone. These variables are essential for evaluating the drying process and understanding how the system evolves over time.

Regarding Temperature and Relative Humidity, three sections are analyzed to generate the following charts: the inlet at $y = 0$, the mid-height at $y = 0.6$ meters, and the outlet at the top of the meshgrid. For calculating the drying rate, the mass difference between the inlet and the outlet is used, as explained in the previous chapter.

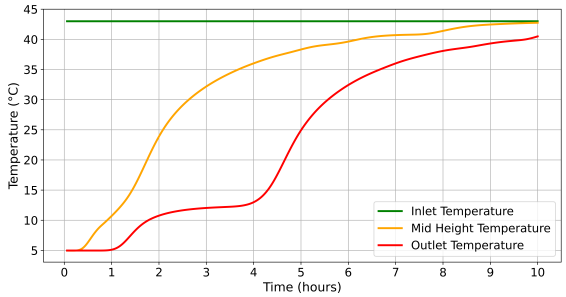

Figure 7.4: Simulation of temperature over time, showing the inlet temperature remaining constant and the mid-height and outlet temperature gradually increasing

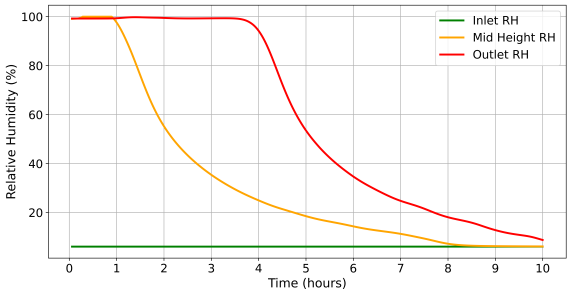

Figure 7.5: Simulation of the relative humidity over time, illustrating the constant inlet humidity and the decreasing mid-height and outlet humidity

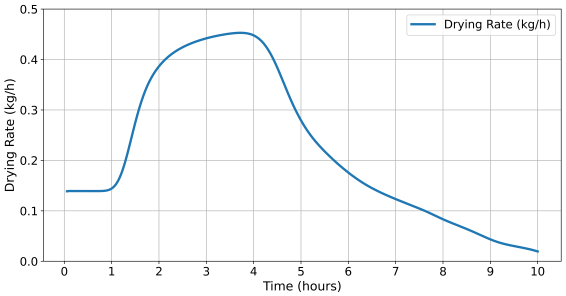

Figure 7.6: Drying rate obtained from the Fluent simulation as a difference of mass flow rates between the inlet and the outlet

The constant inlet air temperature (at $y = 0$) is significantly higher than the ambient temperature due to preheating by the boiler. This preheating is crucial for increasing the efficiency of the drying process, as warmer air has a greater capacity to absorb moisture from the woodchips. Additionally, it results in very low relative humidity at the inlet (around 7%), which is highly beneficial for promoting the rapid evaporation of water from the woodchips.

During the initial phase of the process (approximately the first hour), as the hot air moves through the system, the temperature at the outlet remains relatively stable. This indicates that the air has transferred most of its thermal energy to the woodchips and the moisture within the pile. This period can be classified as the preheating phase, which would last much longer with a higher pile. During this phase, the relative humidity remains highest in the mid-height zone, though it is slightly lower at the outlet. This discrepancy is caused by the recondensation of water vapor in the layers immediately above those where evaporation has occurred.

As the hot air penetrates deeper into the woodchip pile, the bottom layers have already dried, allowing the thermal energy to reach new material, causing the temperature at mid-height ($y = 0.6$) to start rising. The first part of the material to show a noticeable temperature increase is located directly above the channel, while the furthest left section ($x = 0$) is the last to be affected. This is due to the reduced horizontal movement of air along the x-axis, as the channel primarily directs airflow in a vertical direction. This behavior is more clearly illustrated in Figures 7.7 and 7.8, where the contours of these physical values are shown at 30 minutes and one hour, revealing the progress of the drying front with its characteristic curved shape. The drying front marks the boundary where moisture evaporation is actively occurring, separating the dried material from the wet. Its curved form indicates uneven heat and moisture distribution, influenced by the movement of hot air through the pile. After approximately one hour, the outlet starts to be influenced by the incoming hotter air, leading to a gradual increase in the average temperature in this final part of the control volume. This has a positive effect on the drying rate, as hotter air can hold more water vapor, thus accelerating the drying process. This effect is clearly visible in Figure 7.6, where a sharp increase in the drying rate is observed, and in Figures 7.9, where the contours at 2 hours are depicted. The RH at the outlet remains stable, while at mid-height it begins to decrease, indicating that the moisture content below 0.6 meters is no longer sufficient to provide enough water vapor to the air at these elevated temperatures. In other words, part of the drying front has already surpassed this height of the pile. During the period between one and four hours, the outlet temperature shows a slight increase, while the RH remains stable. This leads to a continued rise in the drying rate. In the case of a higher pile, this phase would occur later, and the increase in the drying rate would be slower, as the process would be more prolonged. In fact, the time difference between the spread along

the x-axis and y-axis would become more accentuated, leading to some sections of the pile reaching higher temperatures much earlier than others. The state of the drying front at 4 hours is depicted in Figure 7.10. After 4 hours, the situation changes rapidly. The drying rate drops significantly due to the lack of moisture content in most of the control volume, as the drying front has largely reached the outlet and the temperature is rising in this final section. The temperature rise is also accompanied by a decrease in RH, since the absolute humidity remains nearly constant. This process continues until complete evaporation occurs, with the final hours of drying primarily happening at the furthest point from the channel (i.e., on the left side of the contour plot, which in the main plant corresponds to the section between two channels). The evolution over 6 and 8 hours is depicted in contour Figures 7.11 and 7.12, where the shape of the drying front continues to develop, with the lower layers progressively drying until the upper layers are fully reached. As the drying rate decreases, the time required to complete the drying becomes much longer compared to the earlier stages of the process. In the case of greater water content and a higher pile, as in a real-world scenario, this phase would significantly extend the time needed to fully dry the entire biomass volume.

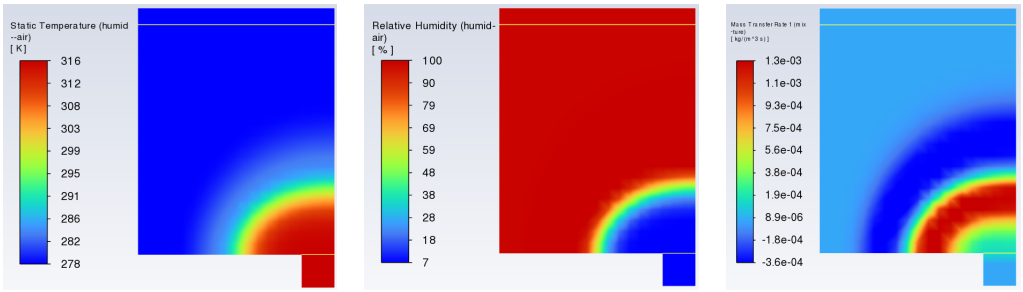

Figure 7.7: Contours of temperature, RH and mass transfer rate at 0.5 hours

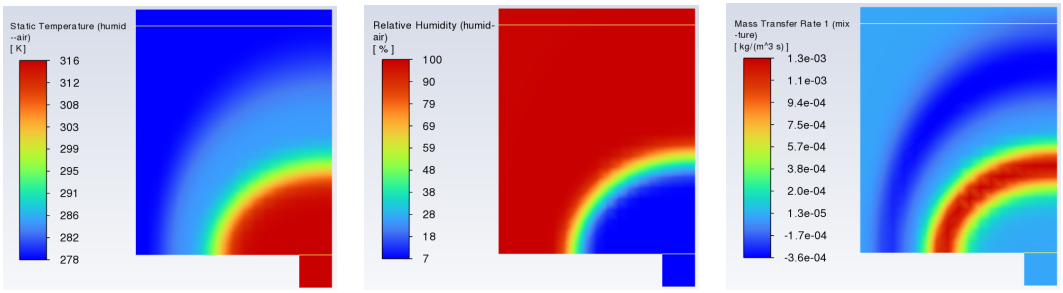

Figure 7.8: Contours of temperature, RH and mass transfer rate at 1 hour

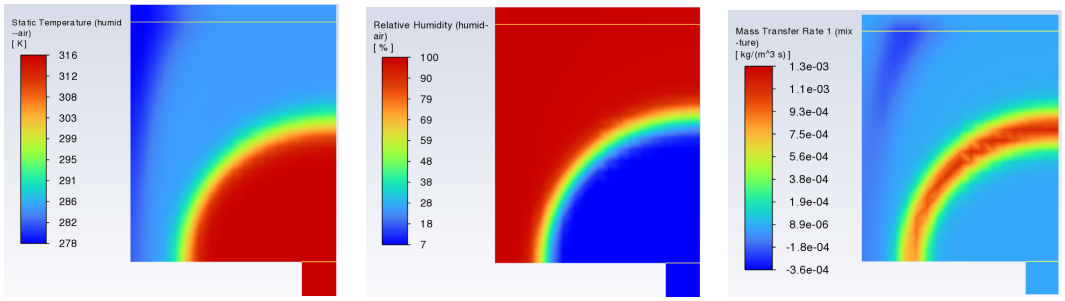

Figure 7.9: Contours of temperature, RH and mass transfer rate at 2 hours

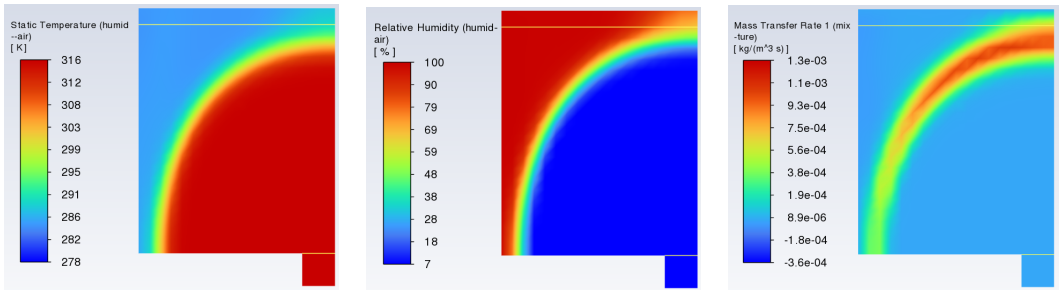

Figure 7.10: Contours of temperature, RH and mass transfer rate at 4 hours

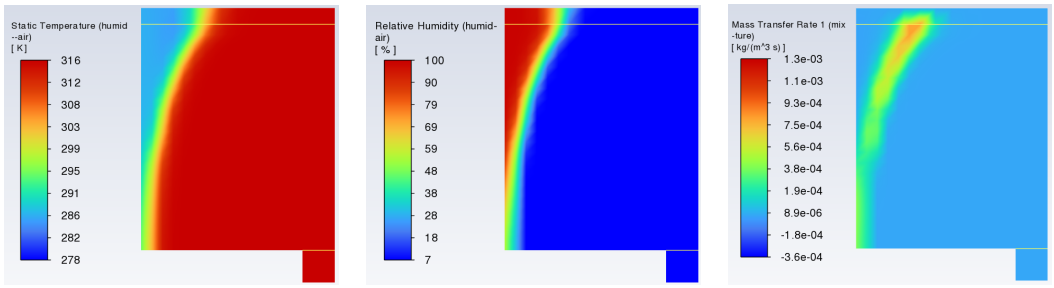

Figure 7.11: Contours of temperature, RH and mass transfer rate at 6 hours

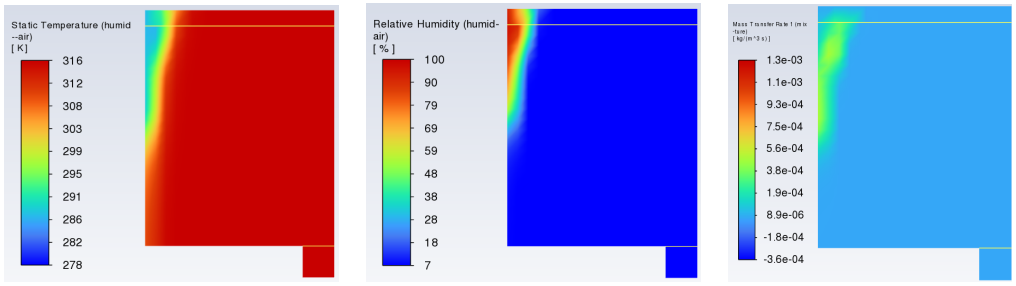

Figure 7.12: Contours of temperature, RH and mass transfer rate at 8 hours

7.8 LHV and Energy Sustainability Index of the Drying Process

The drying process in this system has a direct impact on the Lower Heating Value of the woodchips, which is critical for improving the overall energy efficiency of biomass as a fuel source. The LHV of woodchips decreases with higher moisture content, as a significant portion of the energy is used to evaporate the water within the wood. By reducing the moisture content, the drying process enhances the LHV, making the woodchips more effective for combustion. Dry wood typically has an LHV between 18 and 20 MJ/kg, depending on the type and species of wood. For generic woodchips, an LHV of approximately 19 MJ/kg can be assumed [29]. The LHV of woodchips with a given moisture content (LHV_{wb}) can be calculated using the following equation:

$$LHV_{wb} = LHV_{db}(1 - MC_{wb}) - 2.45\, MC_{wb} \tag{7.6}$$

Where LHV_{db} is the Lower Heating Value of dry biomass, and MC_{wb} is the moisture content of the woodchips, 2.45 represents the heat of vaporization of water in MJ/kg at ambient condition. The Lower Heating Value of the biomass in its "as received" condition is initially 10.2 MJ/kg (MC_{db} equal to 70%). After the drying process, the LHV improves significantly to 14.1 MJ/kg (with an MC_{db} of 30%), resulting in an increase of 3.9 MJ/kg in the energy content. The total amount of woodchips processed during one full cycle of the plant's operation is calculated by multiplying the total available volume of the drying chamber by the bulk density of the woodchips. With a total volume of 972 m^3 and a bulk density of $245\, kg/m^3$, the total mass of woodchips processed in a single cycle is approximately 238 tons. The power input from the boiler is calculated based on the results from the Fluent simulation. In the simulation, the enthalpy of the moist air at the inlet section of the meshgrid, combined with the mass flow rate of the air provides the power available. By multiplying the power at the inlet of the meshgrid by the total number of channels and their entire length, the total netpower available for the drying process is calculated. The result is approximately 162 kW. To determine how many kilograms of woodchips are burned to complete one full drying cycle, values from the literature for the efficiency of industrial woodchip burners with similar power ratings were consulted [30] [31]. At full load, an average efficiency with dry woodchips is assumed to be around 0.85. Assuming the burner in this plant has a similar efficiency, an additional efficiency factor accounting for heat losses through the heat exchanger and channels is considered to be 0.8. Based on the drying time obtained from the Fluent simulation in the previous section, and assuming its constant drying rate phase scales proportionally with the changes in moisture content and the height of the pile, the total drying time is estimated to

be approximately 630 hours, corresponding to 26 days. With this drying time, the amount of woodchips burned during one complete cycle can be calculated using the following formula:

$$m_{burnt} = \frac{P_{available}\, t_{cycle}}{\eta_{burner}\, \eta_{heat\,losses}\, LHV_{wb}} \tag{7.7}$$

where the $P_{available}$ corresponds to 162 kW and t_{cycle} represents the total time required to complete one full drying cycle with this plant. The total mass of woodchips burned is calculated to be 39 tons. By knowing the energy content of the biomass both before and after drying, and the quantity of biomass consumed, it is possible to determine the mass yield in terms of woodchips and the Energy Sustainability Index (ESI). However, it should be noted that this calculation does not include auxiliary systems, except for the fan, which operates at a nominal power of approximately 10 kW and is assumed to be in continuous use. The results are shown in Table 7.5. One of the key metrics in this drying system is

Energy consumed	570 GJ/batch
Increase in Energy Content	927 GJ/batch
ESI	1.6
Mass Yield	0.84

Table 7.5: Summary of energy consumed, increase in energy content, energy sustainability index (ESI), and mass yield for the woodchip drying process based on Fluent simulation results

the mass yield, which refers to the percentage of woodchips that can be effectively used outside of the plant. A portion of the woodchips must be burned as fuel to complete the drying process of the next batch. The remaining woodchips, after the process, are available as a high-quality fuel with improved energy content. This self-sustaining cycle ensures that the plant operates efficiently. The system maintains a high energy efficiency, making it highly effective in converting wet biomass into a dry effective fuel. One of the key advantages of this drying system is its ability to produce high-quality material with a medium to low final moisture content, which significantly improves the LHV of the biomass. The system's ventilation reduces the risk of biodegradation and mass loss, while also ensuring more uniform drying across the woodchip pile. However, the complexity and cost of this system are significantly higher compared to simpler alternatives, such as open drying systems without ventilation, which require only minimal infrastructure. Nonetheless, by optimizing energy efficiency through a controlled drying process, this type of system can effectively enhance the overall energy output from biomass.

This improvement contributes to one of the primary objectives of biomass energy production: maximizing usable energy from renewable resources.

7.9 Conclusions and future work

If the simulated moisture content had been 40%, as desired in the real plant, the drying time would have been substantially longer. This is because a larger difference in moisture content between the initial and final states requires significantly more energy and time for evaporation. Given that the water content would be 40 times greater than the simulated case, it is reasonable to expect a proportional increase in drying time, assuming the drying rate remains constant. Moreover, the increased height of the biomass pile would extend the overall drying time, as the hot air would require more time to penetrate and dry the additional layers of material. In comparison, the drying time for 1 meter of woodchips in this simulation has been shown to be slightly longer than real-world examples of open-air drying [32] [33]. However, this discrepancy can be attributed to several factors not included in the model, all of which contribute to the difference between simulated and real-world results.

A key aspect to consider is the transfer mechanism of moisture from the solid particles to the gas phase, which plays a central role in the drying process. In this simulation, the moisture transfer is modeled based purely on the thermophysical equilibrium between the water vapor in the drying air and the liquid water in the pores of the woodchips. The moisture transfer is further governed by the Lee model, which requires determining an appropriate Lee coefficient. However, this coefficient ideally needs to be calibrated using experimental data that closely matches real-world conditions. For instance, if the Lee coefficient were higher, it would lead to a thinner drying front because the mass exchange between liquid water and vapor would occur more rapidly. This accelerated exchange would also result in a faster consumption of the thermal energy available from the drying air, further influencing the drying dynamics.

Additionally, the model does not account for microbiological activity, which in real situations raises the internal temperature of the woodchip pile, speeding up the drying process. While this effect helps moisture evaporate faster, it also leads to material degradation over time. Another important aspect, is the absence of turbulent airflow in the porous woodchip structure. In reality, turbulence would enhance heat transfer, allowing the water temperature to rise more quickly and promoting faster evaporation.

Furthermore, this simulation assumes uniform thermophysical properties, such as thermal conductivity, moisture content, and heat capacity, for all woodchips. However, parameters like density and heat capacity in Fluent actually vary with moisture content and temperature, and incorporating these variations in future work would provide greater accuracy. In reality, woodchips exhibit considerable variability. They may come from different species of wood or various parts of the tree, such as heartwood, bark, or other sections, each with distinct properties.

Additionally, woodchips vary in size, shape, and moisture content, all of which influence the drying process. Another critical area for improvement is understanding how wood retains water and the amount of energy required to release this moisture beyond the energy needed for evaporation. The diffusion of water from the wood should be taken into account, as it plays a crucial role in determining the rate at which moisture is removed from the wood structure. Addressing these aspects would refine the model's energy consumption estimates and provide more accurate predictions of the drying process. In future work, a more detailed analysis of the drying process in the actual plant, supported by the installation of sensors to monitor key variables such as temperature and relative humidity, would help define and calibrate important model parameters. Incorporating this data, along with addressing complexities like moisture transfer mechanisms, microbiological activity, turbulent airflow, and woodchip variability, would bring the model closer to real-world conditions.

Bibliography

[1] Ayhan Demirbaş. «Biomass resource facilities and biomass conversion processing for fuels and chemicals». In: *Energy Conversion and Management* 42.11 (2001), pp. 1357–1378. ISSN: 0196-8904. DOI: https://doi.org/10.1016/S0196-8904(00)00137-0. URL: https://www.sciencedirect.com/science/article/pii/S0196890400001370 (cit. on p. 3).

[2] Peter McKendry. «Energy production from biomass (part 1): overview of biomass». In: *Bioresource Technology* 83.1 (2002). Reviews Issue, pp. 37–46. ISSN: 0960-8524. DOI: https://doi.org/10.1016/S0960-8524(01)00118-3. URL: https://www.sciencedirect.com/science/article/pii/S0960852401001183 (cit. on p. 3).

[3] Carolyn J. Roos. *Biomass Drying and Dewatering for Clean Heat and Power*. 2013th ed. U.S. Department of Energy. Jan. 2013 (cit. on pp. 4, 5, 7).

[4] William L. Kerr. «Chapter 14 - Food Drying and Evaporation Processing Operations». In: *Handbook of Farm, Dairy and Food Machinery Engineering (Third Edition)*. Ed. by Myer Kutz. Third Edition. Academic Press, 2019, pp. 353–387. ISBN: 978-0-12-814803-7. DOI: https://doi.org/10.1016/B978-0-12-814803-7.00014-2. URL: https://www.sciencedirect.com/science/article/pii/B9780128148037000142 (cit. on p. 6).

[5] Konsta Turunen. «Energy efficiency improvement potential in a paper mill by means of heat load balancing». PhD thesis. Jan. 2017 (cit. on p. 8).

[6] WilliStahlteile. *Open air drying picture*. Accessed on September 1, 2024. 2024. URL: https://www.willi-metallbau.ch/wp-content/uploads/IMG_1747_80x80-1-scaled.jpg (cit. on p. 9).

[7] Raitila J. and Tsupari E. «Feasibility of Solar-Enhanced Drying of Woody Biomass». In: 13 (Mar. 2020), pp. 210–221 (cit. on p. 10).

[8] GLG FARMS. *Wood chip is back on the drying floor*. Accessed on September 1, 2024. 2020. URL: https://www.glgfarms.co.uk/wp-content/uploads/2019/07/img_1124.jpg (cit. on p. 10).

[9] CONA. *Wood Chips Drying*. Accessed on September 1, 2024. 2024. URL: https://www.conasolar.com/en/wood-chips-drying/ (cit. on p. 10).

[10] COOPEOS. *Biomasse locale pour une chaleur durable*. Accessed on June 1, 2024. 2024. URL: https://www.coopeos.be/ (cit. on p. 11).

[11] GROS. *Single intake radial fans 1RV for drying*. Accessed on June 20, 2024. 2024. URL: https://gros.si/en/trgovina/drying-fans/single-sided-suction-fans-1rv-for-drying-hay-bales-grain-corn-fruit-hay/ (cit. on p. 15).

[12] Peter Bengtsson and Johan Claesson. *Modeling the drying of porous material*. 2009 (cit. on pp. 17–19, 21, 51).

[13] Forest Products Laboratory. *Wood handbook: wood as an engineering material*. 1999. DOI: 10.2737/fpl-gtr-113. URL: http://dx.doi.org/10.2737/FPL-GTR-113 (cit. on pp. 18, 19, 21).

[14] Józef Horabik et al. «Breakage Strength of Wood Sawdust Pellets: Measurements and Modelling». In: *Materials* 14 (June 2021), p. 3273. DOI: 10.3390/ma14123273 (cit. on pp. 18, 19, 51).

[15] Gabriel M. Johnson, Reid D. Christianson, Richard A.C. Cooke, Carolina Díaz-García, and Laura E. Christianson. «Denitrifying bioreactor woodchip sourcing guidance based on physical and hydraulic properties». In: *Ecological Engineering* 184 (2022), p. 106791. ISSN: 0925-8574. DOI: https://doi.org/10.1016/j.ecoleng.2022.106791. URL: https://www.sciencedirect.com/science/article/pii/S092585742200252X (cit. on p. 19).

[16] Matthew T. Amato, Daniel Giménez, Sarat Kannepalli, Peter F. Strom, Uta Krogmann, and Robert J. Miskewitz. «Forecasting leachate generation from pilot woodchip stockpiles using a three-dimensional transient flow model». In: *Journal of Environmental Management* 262 (2020), p. 110379. ISSN: 0301-4797. DOI: https://doi.org/10.1016/j.jenvman.2020.110379. URL: https://www.sciencedirect.com/science/article/pii/S0301479720303145 (cit. on pp. 19, 51).

[17] Vandana Subroy, Daniel Giménez, Mingming Qin, Uta Krogmann, Peter F. Strom, and Robert J. Miskewitz. «Hydraulic properties of coarsely and finely ground woodchips». In: *Journal of Hydrology* 517 (2014), pp. 201–212. ISSN: 0022-1694. DOI: https://doi.org/10.1016/j.jhydrol.2014.05.025. URL: https://www.sciencedirect.com/science/article/pii/S0022169414003898 (cit. on p. 19).

[18] Markku J. Lampinen. *Thermodynamics of humid air*. Translated by Juho Arjoranta, accessed on September 10, 2024. URL: https://mycourses.aalto.fi/pluginfile.php/1919916/mod_resource/content/1/Thermodynamics_of_humid_air.pdf (cit. on pp. 22, 23).

[19] Inc. ANSYS. *Ansys Fluent User's Guide 2024 R1*. 2024th ed. Ansys Fluent. Jan. 2024 (cit. on pp. 25, 32, 36, 37, 51, 56).

[20] Nicolas Parmentier. «Experimental characterization and numerical simulation of packed beds of wood particles». PhD thesis. Universite catholique de Louvain, Jan. 2015 (cit. on p. 25).

[21] Tomáš Blejchař, Jiří Raška, and Jana Jablonská. «Mathematical Simulation of Drying Process of Fibrous Material». In: *EPJ Web of Conferences* 180 (Jan. 2018), p. 02010. DOI: 10.1051/epjconf/201818002010 (cit. on pp. 26, 30).

[22] Inc. ANSYS. *Ansys Fluent Theory Guide 2024 R1*. 2024th ed. Ansys Fluent. Jan. 2024 (cit. on pp. 26–31, 34, 36).

[23] W. H. Lee. «A Pressure Iteration Scheme for Two-Phase Flow Modeling». In: 2002. URL: https://api.semanticscholar.org/CorpusID:124568808 (cit. on p. 31).

[24] M. Mayerhofer, J. Govaerts, N. Parmentier, H. Jeanmart, and L. Helsen. «Experimental investigation of pressure drop in packed beds of irregular shaped wood particles». In: *Powder Technology* 205.1 (2011), pp. 30–35. ISSN: 0032-5910. DOI: https://doi.org/10.1016/j.powtec.2010.08.006. URL: https://www.sciencedirect.com/science/article/pii/S0032591010003980 (cit. on p. 34).

[25] Peter Bengtsson. «Experimental Analysis of Low-Temperature Bed Drying of Wooden Biomass Particles». In: *Drying Technology* 26 (May 2008), pp. 602–610. DOI: 10.1080/07373930801946726 (cit. on pp. 35, 39–43, 46).

[26] Rajesh Bhaskaran and Lance Collins. «Introduction to CFD basics». In: *Cornell University-Sibley School of Mechanical and Aerospace Engineering* (2002), pp. 1–21 (cit. on pp. 36, 37).

[27] European Commission. *Photovoltaic Geographical Information System (PVGIS)*. Accessed on June 10, 2024. 2022. URL: https://re.jrc.ec.europa.eu/pvg_tools/en/ (cit. on p. 53).

[28] *Solid biofuels — Determination of moisture content — Oven dry method*. Standard. Brussels, BE: EUROPEAN COMMITTEE FOR STANDARDIZATION, Jan. 2009 (cit. on p. 53).

[29] Stefan Döring. *Power from Pellets: Technology and Applications*. Feb. 2011, pp. 1–223. ISBN: 978-3-642-19961-5. DOI: 10.1007/978-3-642-19962-2 (cit. on p. 62).

[30] Hargassner. *Wood chip boiler*. accessed on September 20, 2024. URL: https://www.hargassner.com/uk-en/boilers/wood-chip-boiler/boiler-eco-hk-250-330-kw/ (cit. on p. 62).

[31] ETA. *ETA wood chip boiler HACK VR 250 to 500 kW*. accessed on September 20, 2024. URL: https://www.eta.co.at/en/products/product-overview/wood-chips/eta-hack-vr-333-500-kw/ (cit. on p. 62).

[32] Carsten Lühr, Ralf Pecenka, Hannes Lenz, and Thomas Hoffmann. «Cold air ventilation for cooling and drying of poplar wood chips from short rotation coppice in outdoor storage piles in Germany». In: *Biomass and Bioenergy* 146 (2021), p. 105976. ISSN: 0961-9534. DOI: https://doi.org/10.1016/j.biombioe.2021.105976. URL: https://www.sciencedirect.com/science/article/pii/S0961953421000131 (cit. on p. 65).

[33] *Woodchip Drying*. Standard. Scotland, UK: Forestry Commission Scotland, Apr. 2011 (cit. on p. 65).